Author/s:
Hallenberger, M;Reuning, L;Back, S;Gallagher, SJ;Iwatani, H;Lindhorst, K

Title:
Climate and sea-level controlling internal architecture of a Quaternary carbonate ramp (Northwest Shelf of Australia)

Date:
2022-04-01

Citation:
Hallenberger, M., Reuning, L., Back, S., Gallagher, S. J., Iwatani, H. & Lindhorst, K. (2022). Climate and sea-level controlling internal architecture of a Quaternary carbonate ramp (Northwest Shelf of Australia). Sedimentology, 69 (3), pp.1276-1300. https://doi.org/10.1111/sed.12948.

SEDIMENTOLOGY the journal of the International Association of Sedimentologists

Sedimentology (2021) doi: 10.1111/sed.12948

Climate and sea-level controlling internal architecture of a Quaternary carbonate ramp (Northwest Shelf of Australia)

MAXIMILIAN HALLENBERGER*, LARS REUNING†, STEFAN BACK*, STEPHEN J. GALLAGHER‡, HOKUTO IWATANI§ and KATJA LINDHORST¶
**Energy and Mineral Resources Group (EMR), Geological Institute, RWTH Aachen University, Wuellnerstrasse 2, Aachen 52062, Germany (E-mail: maximilian.hallenberger@emr.rwth-aachen.de)*
†Institute of Geosciences, CAU Kiel, Ludewig-Meyn-Strasse 10, Kiel 24118, Germany
‡School of Earth Sciences, University of Melbourne, 253-283 Elgin Street, Carlton, VIC 3053, Australia
§Division of Earth Science, The Graduate School of Sciences and Technology for Innovation, Yamaguchi University, Yoshida 1677-1, Yamaguchi 753-8511, Japan
¶Institute of Geosciences, CAU Kiel, Otto-Hahn-Platz 1, Kiel 24118, Germany

Associate Editor – Eric Hiatt

ABSTRACT

The continental shelf of Northwest Australia hosts an extensive tropical carbonate ramp that forms an important template for the interpretation of similar systems in the sedimentary record. Yet, little is known about its development from the middle to late Quaternary, a period of high frequency glacioeustatic changes in sea-level and climate. This research describes core and seismic-reflection data from a mid-ramp to outer ramp transect at the Northwest Shelf. Core material includes the upper 70 m of International Ocean Discovery Program Site U1461 (Expedition 356), which covers the last 500 kyr. During arid glacials, sedimentation is characterized by inorganically precipitated carbonates, including aragonite-needle mud and ooids. Ooids developed under shallow marine conditions on small-scale flat-topped platforms. Seismic and sedimentological evidence indicates that these platforms developed locally on top of the present-day mid-ramp and were typically only active during a single glacial period. Aragonite-needle mud precipitated (inorganically) in shallow-water areas. Much of these fine sediments were subsequently exported into deeper water where they mixed with pelagic carbonates. Humid interglacials are generally characterized by reduced sedimentation across the Northwest Shelf of Australia, resulting in the amalgamation of glacial lowstand deposits. Yet, substantial amounts of skeletal carbonates were deposited at the studied location during the Holocene and Marine Isotope Stage 11. These sediment accumulations are interpreted as a local feature caused by a decline in current energy. The study presented highlights a ramp system where climate is as important as sea-level in controlling carbonate deposition.

Keywords Aragonite-needle mud, Australian Shelf, distally steepened ramp, lowstand shedding, ooids, Northwest Shelf.

INTRODUCTION

The production, accumulation and export of carbonates are controlled by parameters that are either internal (autogenic) or external (allogenic) to the observed shallow marine system. The resulting carbonate deposits might reveal strong cyclicity in response to the rhythmic nature of the underlying controlling factors. For Quaternary systems, glacioeustatic changes in relative sea-level (allogenic factor) are certainly one of the most appreciated influences in determining the capacity of a carbonate factory (cf. Schlager, 2003) to produce and export material. This importance is based on the fundamental nature of tropical carbonate platforms as shallow marine areas, where production is strongly tied to the photic zone. This effect is most pronounced on isolated flat-topped carbonate platforms (for example, the Bahamas: Purdy, 1963; Swart *et al.*, 2009) or rimmed shelfs (for example, Belize: Gischler, 1994; Gischler, 2003), where even slight drops in sea-level may expose large portions of the inner platform (Haak & Schlager, 1989; Schlager, 1991). Carbonate production is then shifted to a comparatively small and narrow strip of the former platform slope (Cook & Taylor, 1991). During relative sea-level highstands, large areas of the flat-topped platform are submerged under shallow water resulting in elevated carbonate production (Schlager *et al.*, 1994). High sedimentation rates on the inner platform quickly fill the available accommodation space and drive transportation of shallow-water carbonates into the adjacent basin, where they mix with calcite from pelagic sources (Eberli & Ginsburg, 1987). This elevated production and subsequent export of carbonates is commonly known as ‘highstand shedding’ (Schlager *et al.*, 1994).

A carbonate ramp, by comparison, is defined by a gently dipping shelf (<1°) which either transitions gradually into the adjacent basin (homoclinal ramp; for example, Trucial Coast) or exhibits a distinct offshore slope break (distally steepened ramp; for example, Yucatan Shelf) (Burchette & Wright, 1992). Due to its geometry, facies belts transition gradually with increasing water depth representing a continuous decrease in water energy (Tucker & Wright, 1990). The export of material differs between homoclinal ramps and distally steepened ramps. In the latter, slope deposits are typically composed of fine-grained material redeposited by gravity flows from the outer ramp. Homoclinal ramps generally experience limited redeposition into deeper water, although storm events can play an important role in transporting shoreface sediments to the deeper parts of the ramp (Tucker & Wright, 1990; Burchette & Wright, 1992). Minor changes in relative sea-level experienced by a ramp commonly result in a simple shift of the shallow-water area with little influence on the production or export of carbonates (Burchette & Wright, 1992; Schlager *et al.*, 1994). Major sea-level falls (>100 m), as often experienced during glaciations (Miller *et al.*, 2005), may expose larger parts of the ramp system. As a result, epeiric ramps, such as the Trucial Coast or Shark Bay (Northwest Australia) may become entirely exposed or transform into restricted lacustrine systems (Logan *et al.*, 1970; Purser & Evans, 1973; Burchette & Wright, 1992).

In comparison, little is known about the evolution of tropical Quaternary distally steepened ramp systems, which are situated adjacent to a deeper basin. Nevertheless, carbonate ramps are a common occurrence in the geological record and oftentimes host considerable hydrocarbon or mineral deposits (Burchette & Wright, 1992). Research on modern examples including the Yucatan Shelf (e.g. Ward & Brady, 1973; Rankey *et al.*, 2021) and the Northwest Shelf of Australia (e.g. James *et al.*, 2004), is largely based on present-day seafloor sedimentation and therefore of limited use in predicting the temporal evolution of these systems. The delineation of ramp geometries based on fieldwork is often difficult due to the limited extent of most outcrops. To assess a ramp system in total, interpretation of two-dimensional seismic-reflection data represents an essential tool. However, many ramp systems are too extensive and thin for geometries and stratigraphies to be resolved on standard industry 2D seismic-reflection data (Burchette & Wright, 1992). Thus, there is a need for high-resolution data that allows combining seismic-reflection and borehole analysis to assess the temporal and spatial evolution of these complex and important depositional environments.

In this study, a combination of International Ocean Discovery Program (IODP) core data and high-resolution seismic data are used to investigate the development of the carbonate factory of the Northwest Shelf of Australia (NWS) between the mid-Pleistocene and Holocene. Petrophysical properties (V_p, bulk density, acoustic impedance) are used to link sedimentary facies to reflectors on high-resolution 2D seismic data. This enables a precise interpretation of the geometry, composition and timing of the formation of shelf carbonates. This research further intends to investigate the response of a shallow marine tropical–arid carbonate ramp to internal (autogenic) and external (allogenic) processes and asses their role in the potential formation of cyclical sedimentary patterns. This study contributes to the understanding of the Quaternary NWS and tropical carbonate ramps in general. The results presented are of direct importance for the interpretation of ancient carbonate ramp systems observed on seismic-reflection data and in outcrops.

GEOLOGICAL SETTING

The continental shelf of Northwest Australia (NWS) stretches between *ca* 16°S and 21°S and is located at the transition between the tropical and sub-tropical realms (Fig. 1). The geometry of the shelf is defined by a gentle dipping distally steepened ramp (cf. Read, 1985), which at its widest point spans about 250 km across to the 200 m isobath (James *et al.*, 2004). The ramp can be subdivided based on hydrodynamics into inner ramp (<50 metres water depth – mwd; fair weather wave base), mid-ramp (50 to 120 mwd; storm weather wave base) and outer ramp (>120 mwd) (Burchette & Wright, 1992; James *et al.*, 2004). This study focuses on the westernmost parts of the NWS, located seaward of Barrow Island (Fig. 1). Compared to most of the NWS, this area is defined by a narrower transition between the mid-ramp and outer-ramp, with seafloor inclination increasing rapidly seaward of the 200 m isobath (Jones, 1973; James *et al.*, 2004).

The climate of the NWS is defined by arid conditions with an annual rainfall of about 320 mm (Australian Bureau of Metereology, 2000). Most of this rainfall occurs from February to June during the Australian Summer Monsoon (Hesse *et al.*, 2004). During this period, several otherwise dry river systems transport large amounts of terrigenous material to the shelf, resulting in prominent sediment plumes (Dix *et al.*, 2005). The physical oceanography of the NWS is subjected to open marine conditions characterized by a high-energy environment including swell waves, tropical cyclones and large tides (Jones, 1973; James *et al.*, 2004; Belde *et al.*, 2017).

The sediment distribution on the seafloor is well-documented (Jones, 1973; James *et al.*, 2004; Dix *et al.*, 2005). Modern sedimentation is characterized by photozoan and heterozoan elements at the inner ramp (Dix, 1989; Orpin *et al.*, 1999). The mid-ramp comprises largely heterozoan bioclasts mixed with larger benthic foraminifera, while the outer ramp consists predominantly of hemipelagic sediments and some resilient shelf edge reefs (Jones, 1973; James *et al.*, 2004; Dix *et al.*, 2005). A ubiquitous component of the mid-ramp is the occurrence of ooids, peloids and aragonitic-needle mud, which have formed shortly after the Last Glacial Maximum (James *et al.*, 2004; Dix *et al.*, 2005).

METHODS AND MATERIALS

Sample material

The IODP Site U1461 (20°12.863'S, 115°3.950'E), the basis of this study, is located 100 km north-

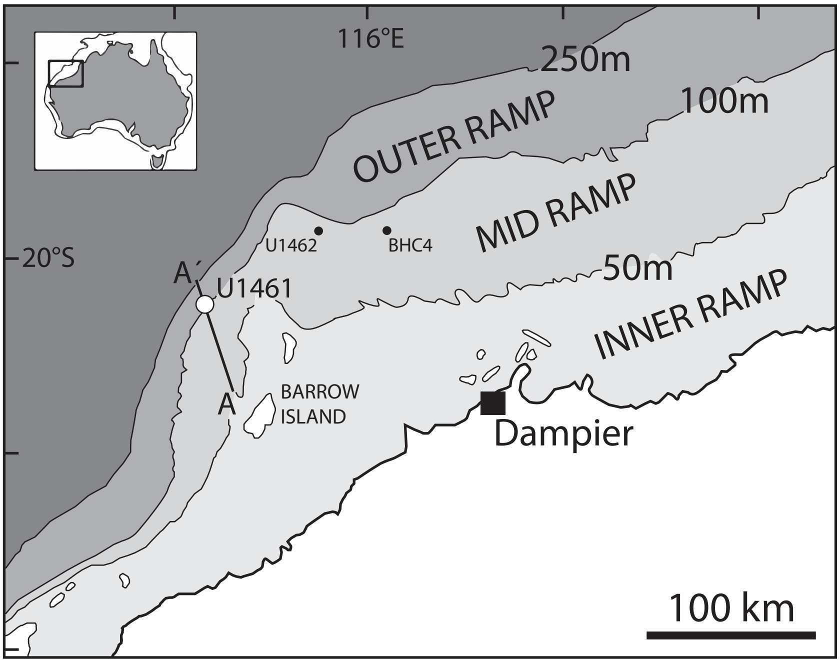

Fig. 1. Map illustrating the ramp division and bathymetry of the Northwest Shelf of Australia (NWS) close to International Ocean Discovery Program (IODP) Site U1461 and important adjoining well sites (modified from James *et al.*, 2004). Further displayed is the location of the analyzed seismic cross-section (A to A′).

west of Barrow Island in the Northern Carnarvon Basin on the shelf edge of a mid-ramp to outer-ramp transition (James *et al.*, 2004; Gallagher *et al.*, 2017b) (Fig. 1). Four IODP boreholes were drilled in close vicinity (<100 m) at a water depth of 127 m (Gallagher *et al.*, 2017b). Three holes (U1461A to U1461C) cored the studied segment from the seafloor to 70 m depth. Core recovery in this interval is around 90% in general, and 100% considering overlap between individual holes at Site U1461. Core samples and petrophysical data have been selected from all three holes to maximize coverage and data quality. The depth of samples and data is expressed as common metres composition depth (CCSF-A) to attribute for shifts between individual holes (IODP-MI, 2011; Gallagher *et al.*, 2017b). Sample denotation follows the IODP guideline outlined as Site/Hole-Core-Section-distance from top (Gallagher *et al.*, 2017a).

Composition and sample mineralogy

In total, 172 samples were collected on shipboard and during the post-cruise sampling party. Sediment composition and fabric were determined using 42 thin-sections under petrographic microscope (Olympus BH-2; Olympus Corporation, Tokyo, Japan). Additionally, 62 samples were wet sieved and dry sieved to investigate sediment based on their size fractions. Mesh sizes include 64 µm, 125 µm, 250 µm and 500 µm. Twelve samples were examined with a scanning electron microscope (SEM; Supra55; Carl Zeiss AG, Oberkochen, Germany) and a coupled energy-dispersive X-ray spectroscope (EDX) to further distinguish sedimentary components and their elemental composition (X-Max 150 Silicon Drift Detector; Oxford Instruments plc, Abingdon, UK).

Mineralogy was determined on 118 samples using a Siemens D5000 X-ray diffractometer (Bruker, Billerica, MA, USA). The measurements of the powdered samples were conducted over an angle field of 66° (4° to 70°) with a step size of $4 \times 10^{-3\circ}$ per second. Standard Rietveld refinement using the software Profex (version 4.0.2) achieved identification and quantification of different mineral phases. Non-destructive determination of mineralogy was achieved by 2D X-ray diffraction (XRD) measurements (D8-Bruker, Bruker, Billerica, MA, USA) following the methodology outlined in Smodej *et al.* (2015) (resident time per spot = 10 min).

X-ray fluorescence (XRF) scanning was performed with an Avaatech XRF core scanner (Avaatech B.V., Dodewaard, The Netherlands) at the JRSO XRF Core Scanning Facility, located at the Gulf Coast Repository in the Texas A&M University Research Park. Scanning resolution is equal to 5 cm down to a depth of 18.5 m after which the resolution reduces to 10 cm. The log ratio of strontium (Sr) to calcium (Ca) is presented as a proxy for relative changes in aragonite content. This relationship is based on the elevated amounts of strontium present in aragonite as compared to calcite (Thomson *et al.*, 2006) and was formerly successfully calibrated against carbonate mineralogy at Site U1461 (Hallenberger *et al.*, 2019).

Geochemical data are complemented by a lightness log, which is a unitless spectrophotometric parameter derived from the reflectance of visible light on split cores (Gallagher *et al.*, 2017a). At Site U1461, lightness of sediments displays a positive correlation with the overall aragonite content, representing a high-resolution proxy with a sampling interval of 2.5 cm (Hallenberger *et al.*, 2019).

Isotope geochemistry

Stable oxygen and carbon isotopes have been studied to better constrain the environmental conditions during the formation of different carbonate facies (Table S1). Analyses were conducted on 38 samples, including non-skeletal grains ($n = 9$) and bulk sediment ($n = 29$). Measurements were carried out at the Institut für Geophysik und Geologie of Leipzig University. Carbonate powders were reacted with 105% phosphoric acid at 70°C using a Kiel IV online carbonate preparation line connected to a MAT 253 mass spectrometer (Thermo Fisher Scientific Inc., Waltham, MA, USA). All carbonate values are reported in per mil (‰) relative to Vienna Pee Dee Belemnite (VPDB) according to the delta notation. Reproducibility was checked by replicate analysis of NBS19 and was better than ±0.025‰ (1σ) for carbon ($\delta^{13}C$) and better than ±0.071‰ (1σ) for oxygen isotopes ($\delta^{18}O$).

Petrophysical properties

Petrophysical properties were measured on shipboard during Expedition 356. P-wave sonic velocity and bulk density were generated with a Whole-Round Multisensor Logger (WRMSL), which simultaneously measures a multitude of petrophysical properties on the encased whole core (Gallagher *et al.*, 2017a). Sonic velocity is defined by the traveltime of 500 kHz ultrasonic waves across the core, whereas bulk density is based on the attenuation of a ^{137}Cs gamma ray beam (Gallagher *et al.*, 2017a). Sonic velocity and density values that are above or below reasonable thresholds were excluded from the data series to reduce the presence of data scatter and to increase the overall data quality. These thresholds follow the recommendations of the shipboard report (Gallagher *et al.*, 2017b). Sonic velocity and density were subsequently multiplied to calculate an acoustic impedance log across the studied interval. Shipboard generated porosity data were utilized to evaluate the influence of sedimentary fabric on acoustic impedance. Porosity was measured on discrete samples collected from the working halves of the core (Gallagher *et al.*, 2017a).

Seismic data

This study utilizes seismic-reflection line SO-259 that was obtained during the 2017 cruise of the *R/V Sonne* (SO257) across the NWS. The high-resolution multichannel seismic-reflection profile was generated with a Mini GI-Gun (1.7 l) and signals were received by a Geometrics GeoEel Streamer system (Geometrics Inc., San Jose, CA, USA). The seismic-reflection data were processed using 2D VISTA seismic processing software (Schlumberger Limited, Houston, TX, USA). The vertical resolution of Line SO-259 is approximately 2.5 m with a maximum penetration of about 500 ms two-way travel time. Time–depth conversion at Site U1461 is based on an IODP (Expedition 356) shipboard generated sonic velocity dataset with a resolution of 5 cm (Gallagher *et al.*, 2017b).

The seismic profile crosses Site U1461 in NNW orientation from Barrow Island to the outer ramp and upper slope transition (Fig. 1). The water depth of this transect ranges from approximately 75 to 185 m. The inclination of the seafloor is low (*ca* 1%) and increases rapidly to up to 18% at the outer ramp to slope transition. The seismic-reflection data are in positive Society of Exploration Geophysicists (SEG) zero-phase polarity, where an increase in acoustic impedance is expressed as a positive amplitude (peak).

Age model

The age model of the top 70 m (CCSF-A) of Site U1461 is based on a combination of radiocarbon ages, biostratigraphic datums and oxygen isotope data (Gallagher *et al.*, 2017b; Hallenberger *et al.*, 2019; Ishiwa *et al.*, 2019b; Courtillat *et al.*, 2020). These datasets were previously compiled into a comprehensive chronological profile (Courtillat *et al.*, 2020), which is in large parts adopted for this research (Fig. 2). For this study, the borehole specific depth scale (CSF-A) of Courtillat *et al.* (2020) was converted to a composite depth scale (CCSF-A), which accounts for differences in depth between holes (Gallagher *et al.*, 2017b).

The material used for radiocarbon dating includes planktonic foraminifera and macrofossils, all of which were cleaned and screened for cementation prior to measurement (Hallenberger *et al.*, 2019; Ishiwa *et al.*, 2019b). In older strata (>40 ka), ages are determined based on coccolithophorid biostratigraphic datums and oxygen isotope data of planktonic foraminifera (Gallagher *et al.*, 2017b; Courtillat *et al.*, 2020). Nannofossil biostratigraphy includes the first occurrence of *Emiliania huxleyi* (18.65 m) and the last occurrence of *Pseudoemiliania lacunosa* (60.73 m). The latter age datum was updated to 430 ka following Raffi *et al.* (2020) (Fig. 2). The only discrepancy with Courtillat *et al.* (2020) is the assigned age for the interval between 15.4 m and 18.65 m depth (see *Discussion*).

RESULTS

Sedimentary composition and distribution

The top 70 m of Site U1461 display a distinct alternating pattern in core colour from dark to light, representing facies related changes in mineralogy (Fig. 3A to H). The mineralogy of the dark-coloured intervals is a mixture of calcite and aragonite with elevated amounts of siliciclastics, while the lighter-coloured intervals are mainly aragonitic with minor siliciclastics (Fig. 3C). Based on texture, the aragonite-rich sections are further subdivided into intervals that contain high amounts of non-skeletal grains and those rich in aragonitic mud (Fig. 3D). Furthermore, a 2 m thick layer of bioclastic grainstone is present in the lower parts of the studied interval. Generally, carbonate content is high throughout the studied section, although slightly lower in dark-coloured sediments (mean = 87%) as compared with lighter-coloured sections (mean = 98%). There is no clear trend in the relative abundance of individual siliciclastic

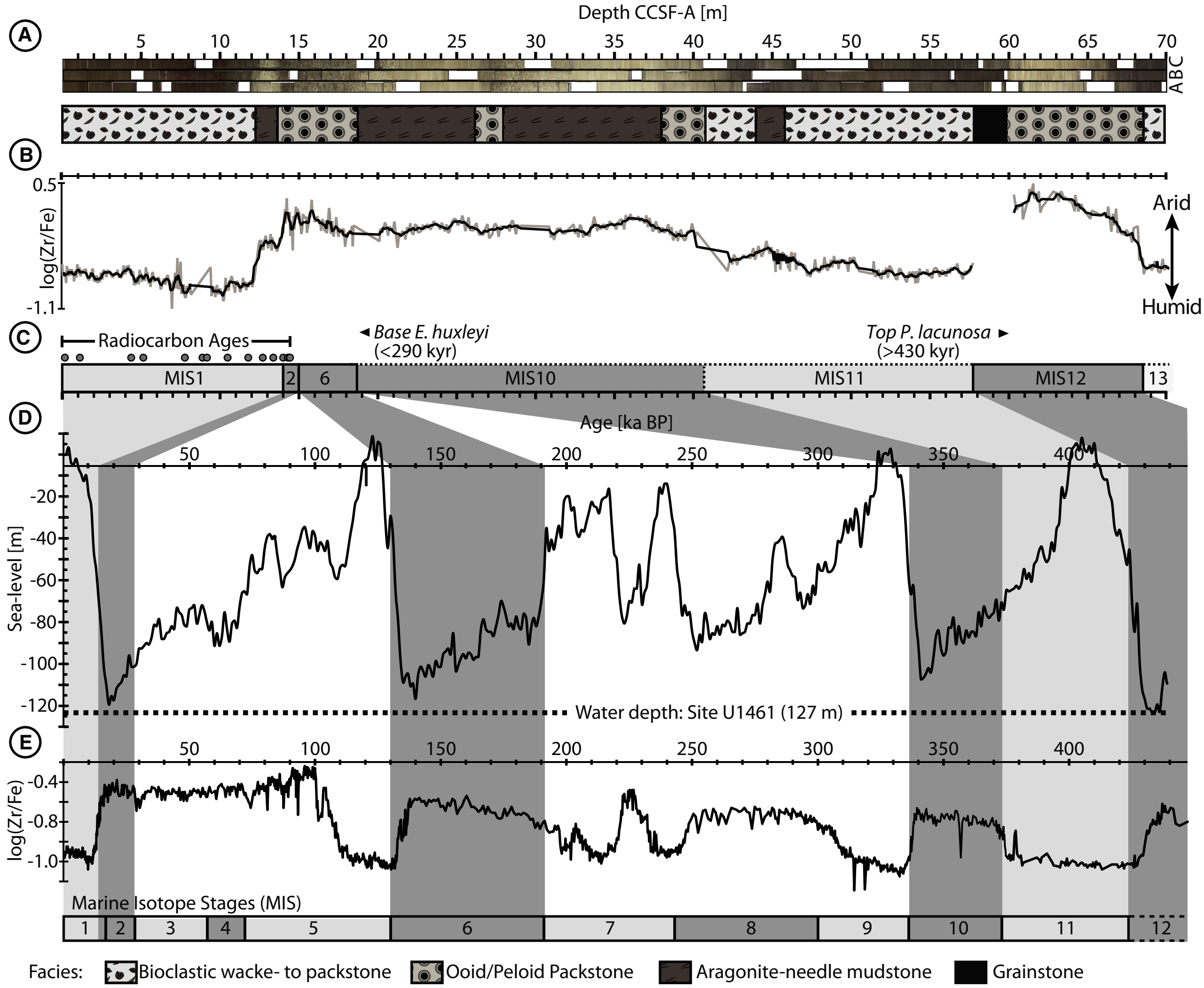

Fig. 2. An age model for the upper 70 m of Site U1461. Depth is expressed as common metres composition (CCSF-A). (A) Core images and facies of holes A to C. (B) The log ratio of zirconium (Zr) over iron (Fe) represents a proxy for arid *versus* humid climate at Site U1461 (Courtillat *et al.*, 2020). (C) Depositional age as indicated by the associated Marine Isotope Stages (MIS). Radiocarbon measurement points are represented by single dots. Sedimentary units are not necessarily representative of the entire MIS they are associated with. (D) Glacioeustatic sea-level curve during the last 450 kyr (Miller *et al.*, 2005). (E) X-ray fluorescence (XRF)-derived log ratio of zirconium (Zr) over iron (Fe) indicates arid versus humid climate offshore Northwest Australia (Stuut *et al.*, 2014).

minerals with depth or between different facies types. Siliciclastic minerals, mainly quartz and feldspars, are therefore presented combined (Fig. 3C).

Facies 1 – Bioclastic wackestone to packstone

Unlithified olive-grey to dark-grey wackestone to packstone represent Facies 1. The mineralogical composition of Facies 1 is a mixture of low-Mg calcite (14 to 49%, mean = 28%), high-Mg calcite (10 to 41%, mean = 28%) and aragonite (17 to 41%, mean = 28%). Additionally, relatively high amounts of siliciclastics (3 to 26%, mean = 13%) are present. They consist of quartz with minor amounts of feldspar (orthoclase and albite) and lithic fragments (Fig. 4A). Minor amounts of dolomite (6 to 12%) occur locally between 41.2 m and 57.8 m. The occurrence of dolomite is accompanied by a comparative decrease of high-Mg calcite and an increase of low-Mg calcite (Fig. 3C). It therefore appears likely that the observed dolomite is a product of high-Mg to low-Mg calcite conversion occurring during early diagenesis. Dolomite of similar age

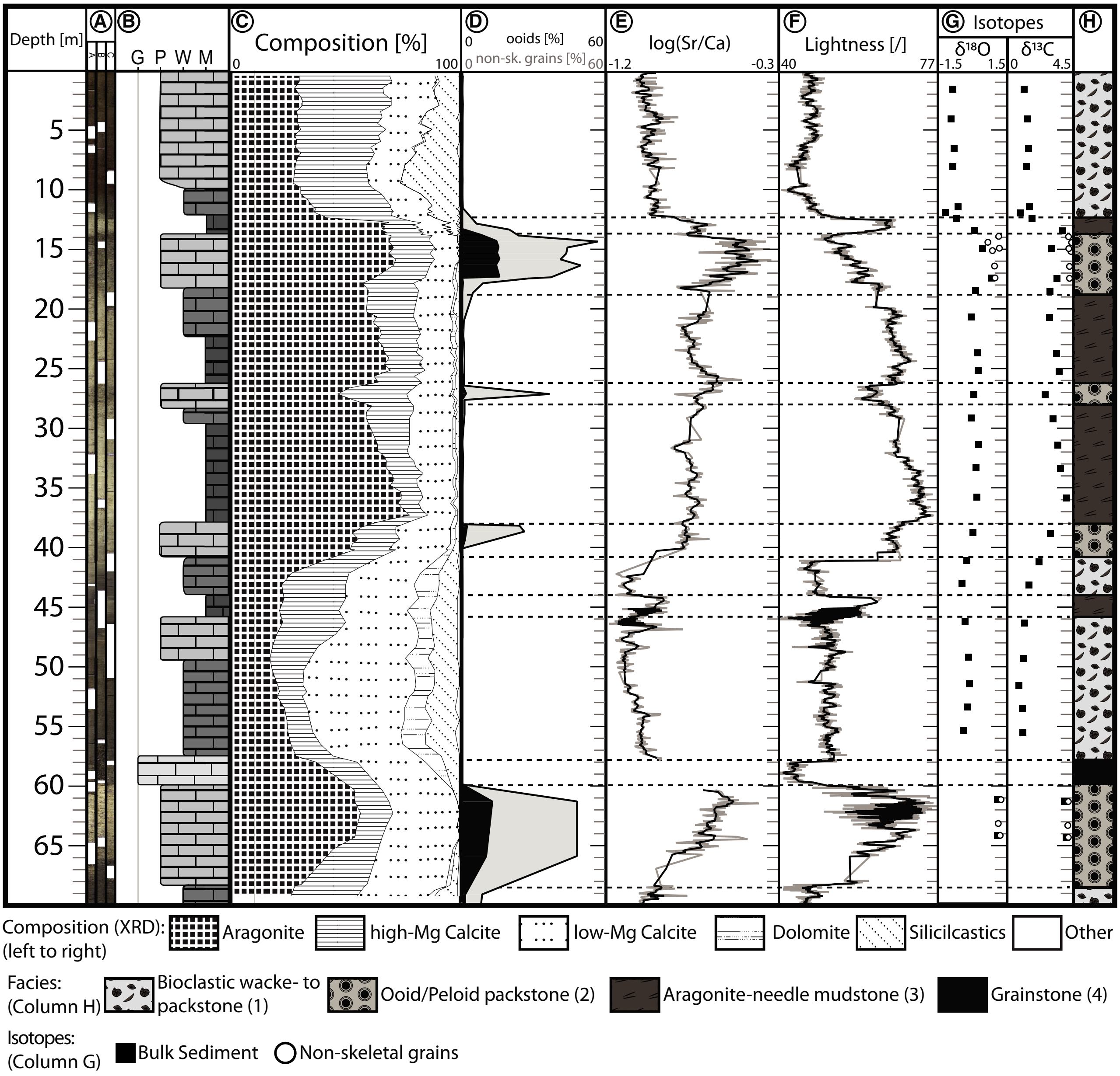

Fig. 3. Facies in the upper 70 m of Site U1461. Depth is expressed as common metres composition (CCSF-A). (A) Core images of holes A to C (from left to right). (B) Dunham classification. (C) XRD-derived cumulative mineralogy. (D) Cumulative abundance of non-skeletal grains and ooids. (E) XRF-derived log ratio of strontium (Sr) and calcium (Ca). (F) Lightness measurements. (G) Oxygen and carbon isotope data. (H) Facies distribution.

and origin was recently described for the Carnarvon Ramp in Southwest Australia (Deik *et al.*, 2019). A detrital origin appears unlikely, because there is no evidence of dolomite occurring within any other parts of the studied section of Site U1461 (Fig. 3C).

Skeletal grains include benthic and planktonic foraminifera, echinoderm spines and fragments, sponge needles, ostracods, gastropod shells, bivalve fragments and bryozoans. Benthic foraminifera have been studied further on a species level, revealing that the assemblage is dominated by *Cibicides lobatulus*, *Gavelinopsis prageri* and *Reussella spinulosa* (Courtillat *et al.*, 2020). Aragonite proxy data, including reflectivity and XRF-derived log ratios of strontium (Sr) and calcium (Ca), are comparatively low and display little fluctuation (Fig. 3E and F). This

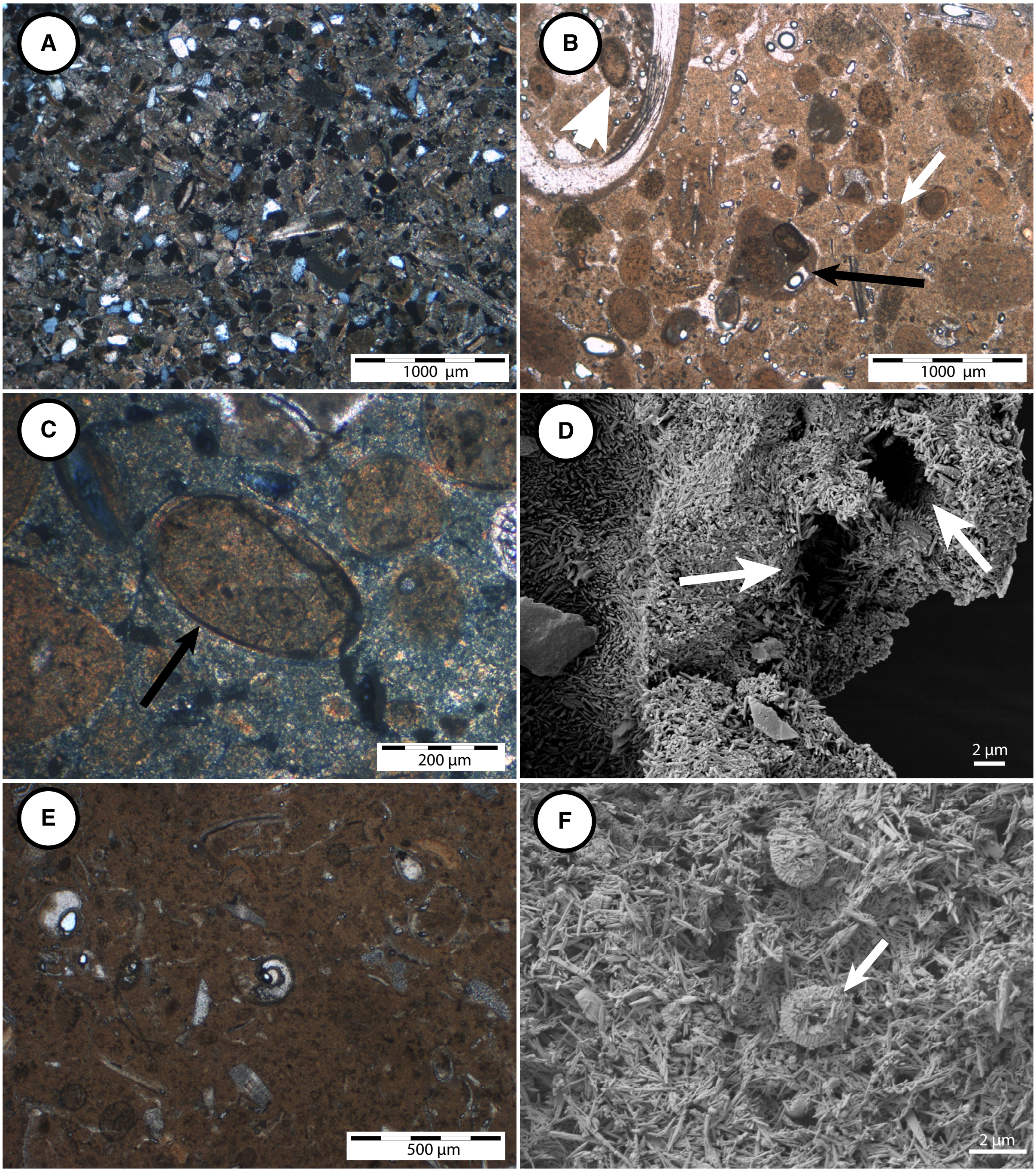

Fig. 4. Representative thin-section and scanning electron microscopy (SEM) images of the three major facies of the upper 70 m of Site U1461. (A) Facies 1 consists of skeletal grains as well as detrital grains including quartz, lithic fragments and feldspar, U1461C-5H-5W-40 cm, crossed polarized light (XPL). (B) Facies 2 is characterized by the high abundance of non-skeletal grains. Non-skeletal grains present are spherical light and dark peloids (white arrow), superficial ooids and intraclasts (black arrow), U1461C-2H-5W-44 cm, plane polarized light (PPL). (C) Some peloids are surrounded by a superficial layer of aragonite, often comprising several cortices (black arrow), U1461C-2H-5W-44 cm, XPL. (D) SEM image along the fractured surface of a peloid. Peloids are almost entirely composed of small (1 to 2 µm) aragonite needles of equal appearance to those in aragonite mud-rich sediments. Larger needles are cementing pores and borings in the peloid (white arrow), U1461C-2H-5W-94 cm. (E) Facies 3 is composed of aragonite mud with minor contribution of skeletal grains, U1461C-3H-2W-44 cm, PPL. (F) The fine fraction (<64 µm) of Facies 3 is composed of small aragonite needles and occasional coccolithophorid plates (white arrow), U1461C-3H-3W-94 cm.

supports the overall reduced amounts of aragonite present in Facies 1, as indicated by XRD measurements. Based on the above outlined criteria, Facies 1 can be identified to occur from 0 to 12.4 m, between 41.2 to 57.8 m, and at the end of the studied interval below 68.5 m (Fig. 3H).

Facies 2 – Ooid/peloid packstone

Sediments of Facies 2 consist of unlithified light grey to grey packstone. The mineralogy is dominated by aragonite (57 to 78%, mean = 66%), with lesser amounts of low-Mg calcite (12 to 25%, mean = 16%) and high-Mg calcite (6 to 23%, mean = 14%). Siliciclastic content is comparatively low (1 to 7%, mean = 2%) (Fig. 3C). Accessory minerals include pyrite, phosphates and glauconite, which are often enriched in non-skeletal grains (Figs 4B and S1). Sediment is composed of non-skeletal grains (50 to 70%) and varying amounts of bioclasts (Fig. 4B and C). Non-skeletal grains include peloids (dark and white), ooids and intraclasts (Fig. 4B). These range in size between 100 to 1500 µm, with most peloids and ooids between 150 to 250 µm. Peloids are commonly of ovoid to spheroid shape and are devoid of any internal structure, albeit some contain fine-grained skeletal debris or detrital components. In general, peloids are almost entirely composed of aragonite needles (Fig. 4D). Single needles are 1 to 2 µm in size with irregular outlines and blunted to pointed terminations. Larger aragonite needles are present as fillings of borings and holes within the peloids, likely the product of localized cementation (Fig. 4D).

The surface of individual non-skeletal grains ranges from rough to smooth (Fig. 5). The difference in surface morphology is the result of the development of superficial coatings, which are present around peloid cores, thereby forming an ooid (Fig. 4C). Ooids contain several concentric laminations with a cumulative thickness ranging between 20 to 30 µm (Fig. 4B and C). Based on the limited thickness of cortices in relation to the overall diameter, the ooids discovered are termed ‘superficial’ (Simone, 1980). Superficial ooids represent 14 to 16% of the bulk sediment and 30 to 50% of the non-skeletal grains (Fig. 3D). They occur exclusively within the thicker sections of Facies 2 between 13.3 to 18.8 m and 60.2 to 68.5 m (Fig. 3D). Ooids and peloids observed between 13.3 to 15.0 m depth further display varying degrees of dark discolouration. This either affects the entire peloid, resulting in a grey to black colour, or is expressed as dark speckles on an otherwise white surface. The EDX-coupled SEM imaging indicates that the discolouration is caused by the occurrence of iron sulphides and to a smaller degree by organic matter, both of which either are enriched in a marginal layer around the peloid or are finely disseminated throughout the peloid (Fig. S1). Dark peloids commonly co-occur with framboidal pyrite, which fills voids in adjacent skeletal grains. This strongly suggests the involvement of bacterial sulphate reduction as a blackening process of peloids.

In addition to stained non-skeletal grains, comparatively large amounts of intraclasts (*ca* 5%) occur between 13.3 m and 15.0 m. The observed intraclasts range in size between 800 µm and 1500 µm. They are well-rounded and usually comprised of several peloids that are bound together by a carbonate cement. Their overall appearance is comparable to stranded ‘lithic intraclasts’ described for the seafloor along the NWS (James *et al.*, 2004). Skeletal

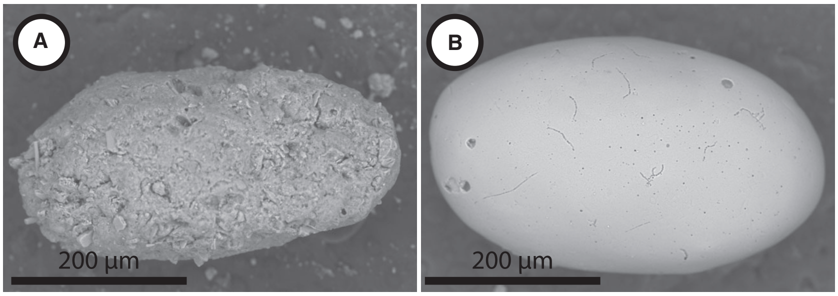

Fig. 5. Scanning electron microscopy (SEM) images of non-skeletal grains present in Facies 2. The surface morphology of single grains ranges between rough (A) to smooth (B), representing faecal pellets and superficial ooids. Ooids further display bioerosion traces. A: U1461B-2H-7W-14 cm. B: U1461B-2H-7W-14 cm.

grains typically include large benthic foraminifera, molluscs (bivalve shells and gastropods), bryozoans and echinoid fragments. Benthic foraminifera mainly include the species *Asterorotalia gaimardii*, *Parrellina verriculata* and *Elphidium craticulatum* (Courtillat *et al.*, 2020).

Additionally, minor intervals of Facies 2 occur within the studied section at 26.2 to 28 .0 m and 38.0 to 41.2 m (Fig. 3H). These thin beds of non-skeletal grain-rich sediments are characterized by an absence of superficial ooids. Instead, non-skeletal grains are entirely composed of peloids with a small admixture of intraclasts (<1%) (Fig. 3D). In addition, pelagic bioclasts such as planktonic foraminifera and pteropods are a common constituent of the fossil assemblage.

Peloids and lithified clasts thereof are interpreted to be primarily faecal pellets. This assessment is based on the mostly uniform ovoid or rod-like shape of peloids as well as their lack of internal structure. The black discolouration of some peloids caused by the occurrence of iron sulphides and organic matter further hints at the biological origin of peloids (Flügel, 2013).

Aragonite proxies generally agree with XRD-derived mineral data, indicating elevated values wherever non-skeletal grain-rich sediments occur. A minor discrepancy is present in Facies 2 at around 13.3 m. There, lightness values suggest a downhole decrease in aragonite content going from aragonite mud into an ooid/peloid packstone (Fig. 3F). This trend is not shown in XRD or XRF data, both of which display a slight increase in aragonite content (Fig. 3C and E). The observed mismatch is likely the result of the occurrence of blackened non-skeletal grains, skewing lightness towards lower values (Fig. 3A).

Facies 3 – Aragonite-needle mudstone

Sediments forming Facies 3 consist of unlithified light-grey mudstone to wackestone. The mineralogy is similar to that of Facies 2, with high aragonite content (40 to 77%, mean = 58%) followed by moderate amounts of low-Mg calcite (2 to 46%, mean = 20%) and high-Mg calcite (6 to 30%, mean = 19%). Siliciclastics only occur in minor amounts (0 to 6%, mean = 2%). However, its composition differs greatly from Facies 2, as it lacks non-skeletal grains (<1%). Facies 3 is instead composed of aragonitic mud (<64 μm) with minor amounts of bioclasts. The aragonitic mud consists almost entirely of small (1 to 3 μm) needle-shaped crystals of equal appearance to those found within peloids (Fig. 4E and F). Bioclasts include planktonic and benthic foraminifera, echinoderm spines, bivalve fragments, ostracods and gastropods. The assemblage of benthic foraminifera is comparable to that of Facies 1 (bioclastic wackestone to packstone), including the occurrence of *C. lobatulus*, *G. prageri* and *R. spinulosa* (Courtillat *et al.*, 2020). However, the most characteristic group of benthic foraminifera consists of the species *Peneroplis pertusus* and *Planispirinella exigua*, which occur exclusively in Facies 3 (Courtillat, 2019). In addition, rare coccolithophorid plates are present in the fine fraction of Facies 3 (Fig. 4F). Facies 3, as outlined above, occurs from 18.8 to 38.0 m and between 12.3 m and 13.3 m.

Facies 4 – Bioclastic grainstone

A unit of grainstone is present from 57.8 to 60.2 m. This interval is only sampled in hole B and represented by a core gap in holes A and C, likely due to a lack of cementation and cohesion of the mud-poor material. No XRD or XRF data has been acquired from this interval. However, based on core observation, Facies 4 can be described as a light greenish-grey grainstone composed of a variety of bioclasts, including gastropods, bivalves, echinoderms, large and small benthic foraminifera, scaphopods, barnacles and lithic clasts.

Stable isotopes

Measurements of bioclastic wackestone to packstone (Facies 1) display $\delta^{18}O$ values ranging between −1.2‰ and −0.1‰ (mean = −0.6‰) and $\delta^{13}C$ between +0.8‰ and +1.7‰ (mean = +1.2‰) (Fig. 6). Comparatively higher values are measured in bulk samples of ooid/peloid packstone (Facies 2), with $\delta^{18}O$ ranging from −0.3 to +1.1‰ (mean = +0.4‰) and $\delta^{13}C$ varying between +2.2‰ and +4.0‰ (mean = +3.1‰) (Fig. 6). Facies 2 further displays a bimodal distribution of measured isotope values. Comparatively heavier values in $\delta^{18}O$ and $\delta^{13}C$ are observed in Facies 2, where ooids are a common sedimentary component. Thinner beds of Facies 2, which do not contain any ooids, display lighter isotope values (Fig. 3).

Non-skeletal grains plot in a relatively narrow window with $\delta^{18}O$ values ranging from +0.7 to +1.2‰ (mean = +1‰) and $\delta^{13}C$ varying between +4.1‰ and +4.4‰ (mean = +4.3‰). Measurements solely of non-skeletal grains are therefore heavier in oxygen and carbon isotope values as compared with bulk measurements of the same facies (Fig. 6). Aragonite-needle mudstones (Facies 3) display similar values to those

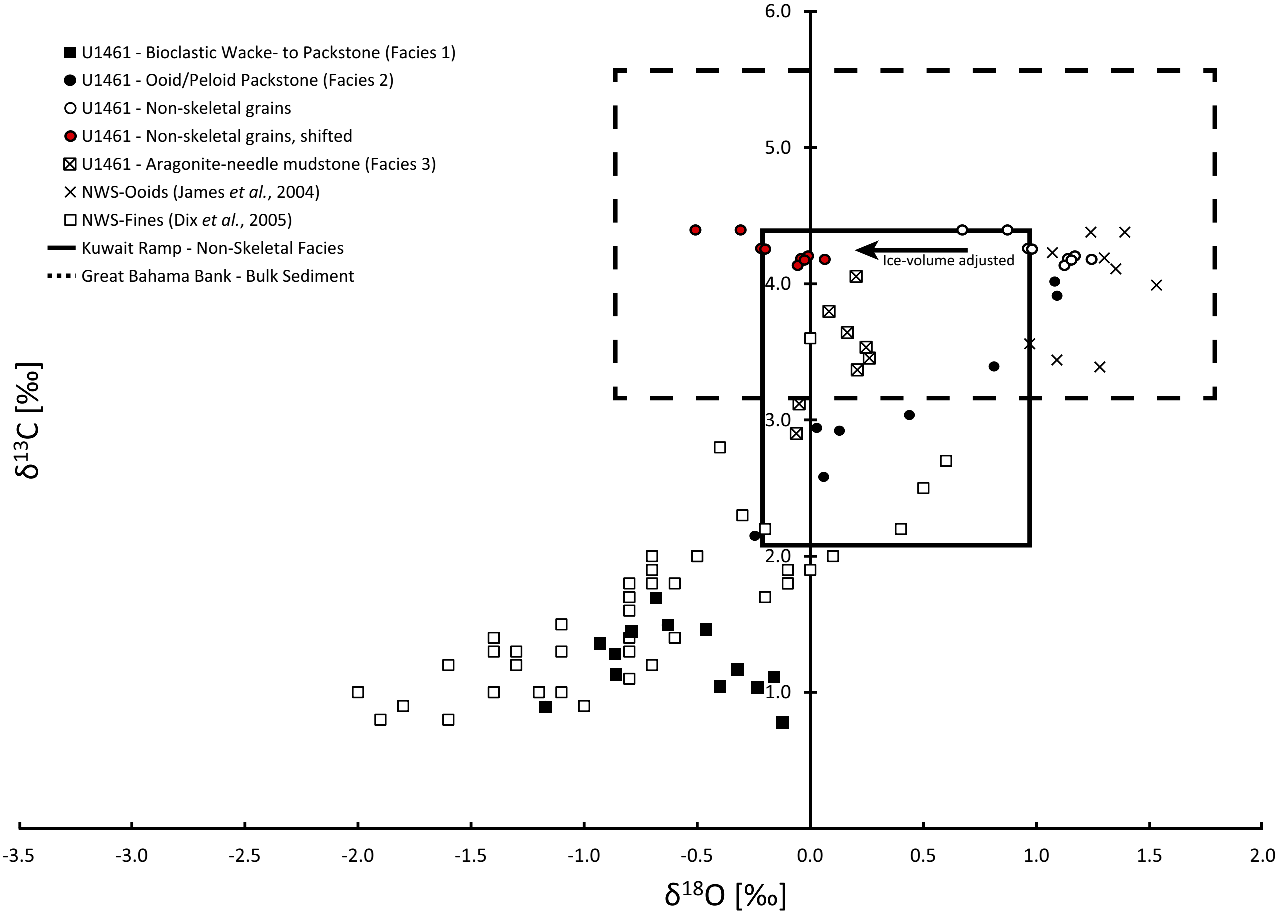

Fig. 6. Oxygen and carbon isotope composition of samples collected at Site U1461. Presented isotope data also includes aragonite mud (Dix *et al.*, 2005) and ooids (James *et al.*, 2004) found at the seafloor of the Northwest Shelf of Australia (NWS) as well as non-skeletal grain facies and ooids deposited on the present-day Kuwait Ramp (Gischler & Lomando, 2005) and the Great Bahama Bank (Swart *et al.*, 2009).

observed in smaller peloid packstone sections, with δ^{18}O values ranging from −0.1 to +0.3‰ (mean = +0.1‰) and δ^{13}C varying between +2.9‰ and +4.1‰ (mean = +3.5‰) (Fig. 6).

Core to seismic integration

The bulk density and sonic velocity log were multiplied to calculate the acoustic impedance over the entire studied depth segment (Fig. 7A to F). Bulk density is a function of grain density (i.e. mineralogical composition) and porosity while sonic velocity is influenced by porosity and pore type. Porosity displays a significant negative correlation ($r = -0.9$, $P = 6.033 \times 10^{-16}$) with acoustic impedance (Fig. S2). It explains 82% of the variation observed in acoustic impedance ($r^2 = 0.8$). In contrast, grain density calculated from the sample mineralogy shows no significant correlation ($r = -0.17$, $P > 0.05$) with acoustic impedance (Fig. S2).

Facies related changes in porosity are the defining factor for acoustic impedance changes within the studied section of Site U1461. Several facies boundaries cause large acoustic impedance contrasts that can be correlated to seismic reflectors, allowing a direct correlation between core and seismic-reflection data (Fig. 7G).

Two-dimensional seismic interpretation

The seismic section (Fig. 8) includes three prominent horizons defined by reflection terminations, which are interpreted as unconformities (U1 to U3; Fig. 8). In the proximal area, these boundaries are defined by a highly

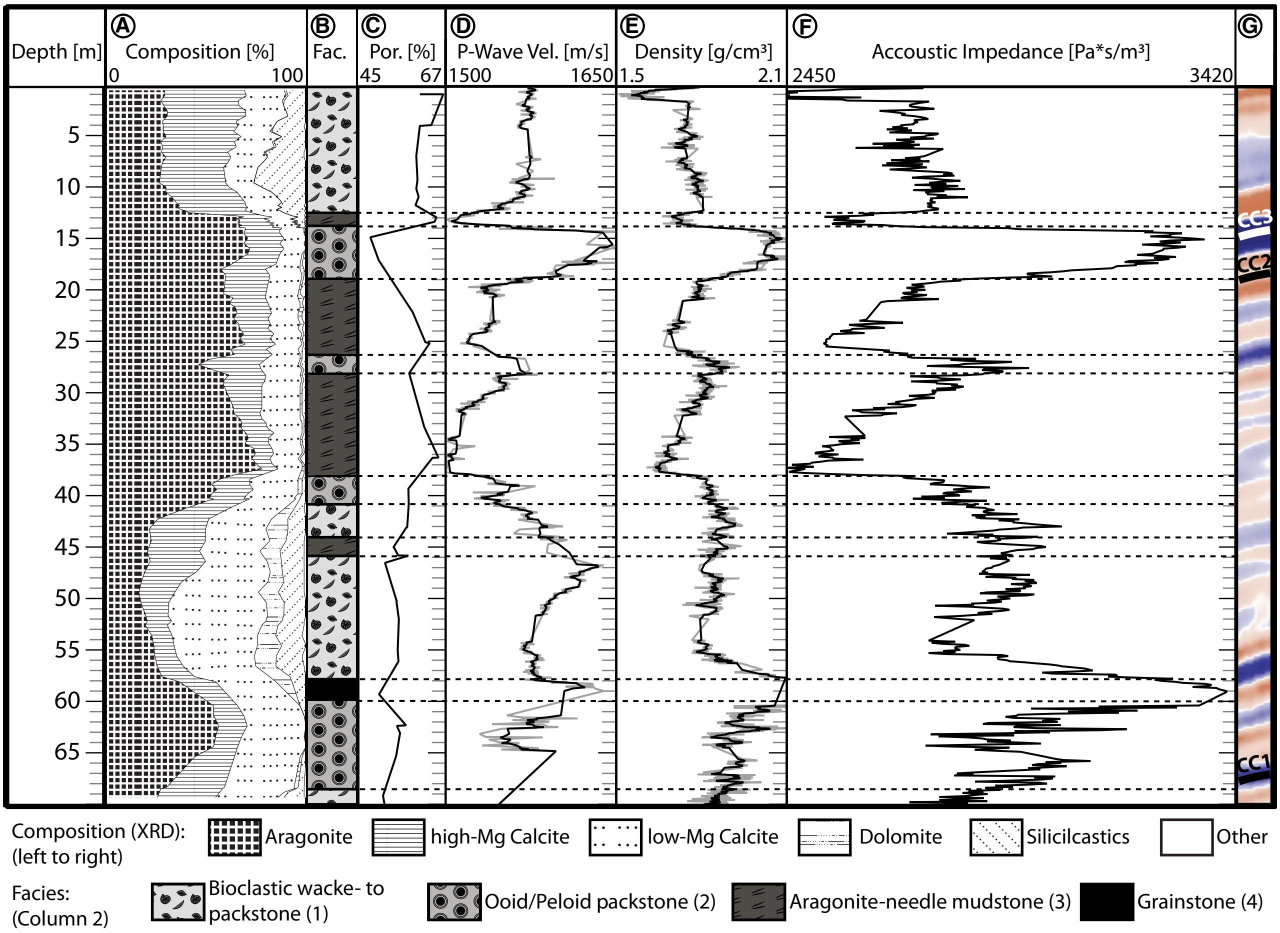

Fig. 7. Summary of petrophysical properties of the upper 70 m of Site U1461. Depth is expressed as common metres composition (CCSF-A). (A) X-ray diffraction (XRD) derived cumulative mineralogy. (B) Facies distribution. (C) Porosity of sediment samples. (D) Sonic velocity measured on whole cores. (E) Bulk density measured on whole cores with gamma ray attenuation. (F) Calculated acoustic impedance values. (G) Seismic trace along the well track converted to depth. Blue represents a positive amplitude (peak) and red a negative amplitude (trough). Additionally displayed are the positions of correlative conformities (CC) as interpreted in seismic.

serrated and irregular morphology as well as the frequent truncation of reflectors underlying each contact. Seaward, the unconformities transition into correlative conformities (CC1 to CC3; Fig. 8), onto which overlying reflectors partially onlap (Fig. 8). At Site U1461, correlative conformities are represented by the two horizons of ooid-rich sediments. In seismic, these units have a wedge-like geometry, with internal downlap and progradation of single sigmoidal reflectors (Platforms 1 and 2; Fig. 8). A similar wedge-like geometry is present in the proximal parts of the seismic line (Platform 3; Fig. 8). This unit lies between two unconformities (U3 and U2; Fig. 8) and includes several high amplitude reflectors.

Typically, the downcore change to non-skeletal grain-rich sediments is associated with positive high-amplitude reflectors caused by a facies related increase in acoustic impedance (Fig. 7). This is also true for the minor occurrences of non-skeletal grains, which are represented by single reflectors without any distinctive geometry (Fig. 8). Thicker intervals, which are dominated by bioclastic sediments (Facies 1) and aragonite mudstones (Facies 3), typically display parallel, medium-amplitude reflectors with diffuse contacts. This is attributed to the relatively homogenous nature of these sediments, especially the aragonite mudstones. The reflector continuity of this seismic unit decreases landward. Medium amplitudes and

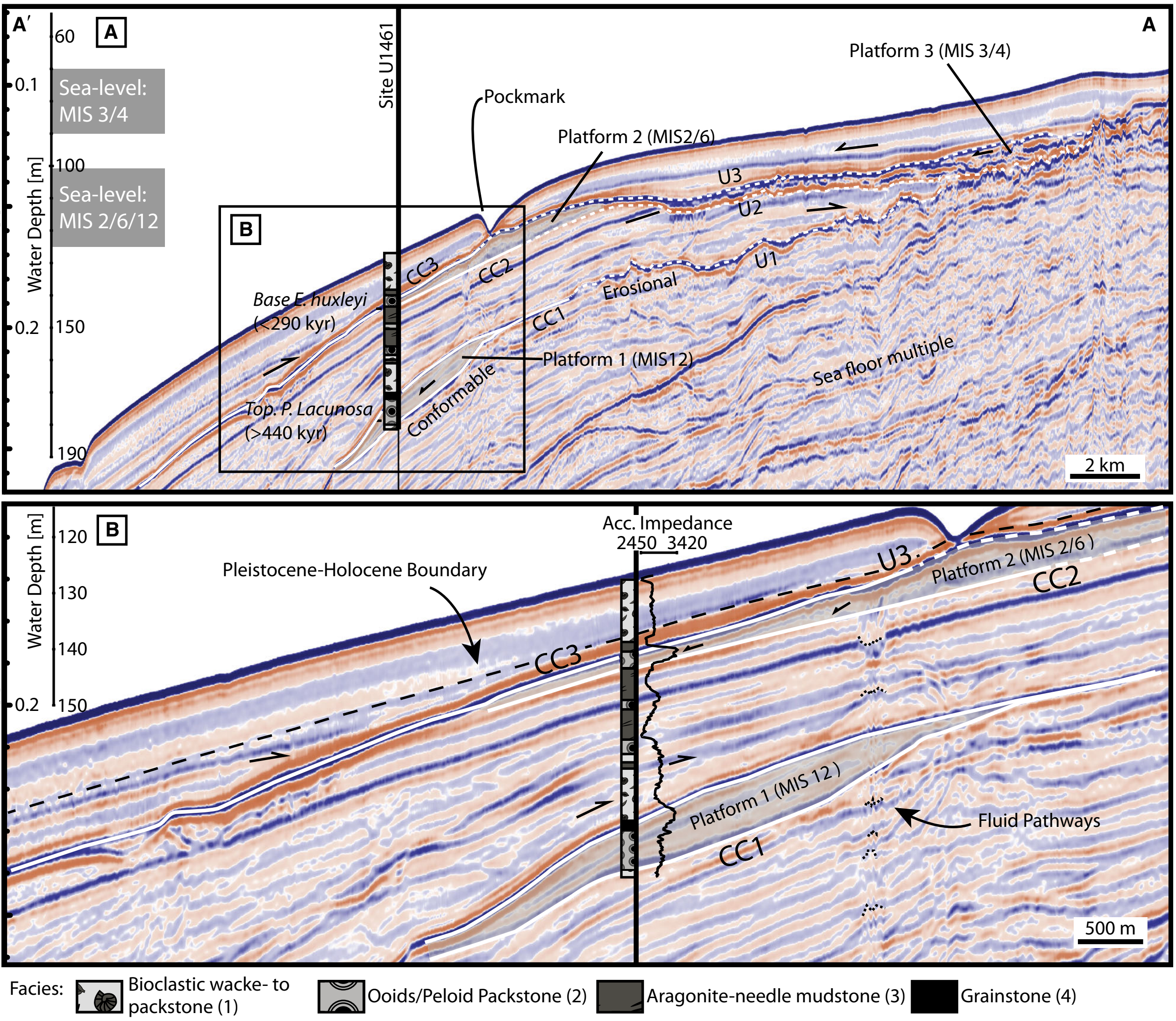

Fig. 8. SSE–NNW oriented seismic-reflection line crossing Site U1461 (A) and associated zoom-in along the well track of Site U1461 (B). The seismic is shot in positive SEG zerophase, where an increase in acoustic impedance is expressed as positive (blue) amplitude. The vertical exaggeration is equal to 93 and 43 times for the upper and lower image, respectively. (A) Several reflectors are truncated landward by unconformities (U), indicating extended periods of subaerial exposure. Seaward, unconformities transition into correlative conformities (CC). (B) Changes in the core based acoustic impedance log are well reflected.

low continuity characterize reflections found between the two older unconformities (U1/U2). Further, reflections are oftentimes non-parallel and display irregular reflector outlines. Landward, reflectors associated with both facies are either truncated by unconformities or display onlap terminations. These onlaps are typically located directly above or against the two distal platforms (Platforms 1 and 2; Fig. 8B). An exception is found in the proximal youngest parts of the seismic section, where reflectors overlying an unconformity (U3) display prominent downlap terminations (Fig. 8).

The seafloor exhibits a depression located just landward of Site U1461 (Fig. 8). In map view, the feature is lens-shaped and approximately 1.5 km long and 400 m wide. The long axis of the groove is oriented roughly north-east/south-west, cutting Line SO257 at a 90° angle. On the seismic-reflection data, it is spatially associated with a seismic discontinuity zone potentially related to vertical fluid migration (Fig. 8). The dimensions and the close-proximity to an underlying possible gas-seep indicate that the morphological feature may represent a pockmark. Pockmarks typically occur due to the rapid venting of a gas and/or fluid and have been described for several locations across the NWS seafloor (Hengesh *et al.*, 2013). The elongated shape of this commonly roundish feature is likely the result of scouring by bottom currents, following the initial creation of the pockmark. This interpretation matches the dominant local current direction, which is parallel to the long axis of the scoured pockmark (Condie & Andrewartha, 2008).

INTERPRETATION AND DISCUSSION

An update to the age model of Site U1461

The comprehensive age model of Site U1461 by Courtillat *et al.* (2020) proposes continuous sedimentation between Marine Isotope Stage 2 (MIS2) to MIS5d. The MIS2 glacial is assigned to the interval between 14.01 m and 16.53 m and the interval between 16.53 m and 18.65 m corresponds to the period between MIS3 to MIS5d. This interpretation contradicts data presented by Ishiwa *et al.* (2019b), which shows that the age of sediments at 15.42 m is already exceeding the radiocarbon dating limit (>40 ka). Sediments below this depth must therefore be older than MIS2 but younger than 290 ka, as indicated by the first occurrence datum of *E. huxleyi* at 18.65 m (Fig. 2).

The sedimentary composition of carbonates found between 15.42 m and 18.6 m is characterized by the abundance of ooids (Fig. 3). Considering the sea-level variability during this period (Fig. 2), the shallow water depth necessary for ooid formation (<10 m) (Simone, 1980) existed only briefly during the later stages of the MIS6 lowstand. This assignment is consistent with a positive peak in oxygen isotope values of *G. menardii* (16.53 m) and the benthic foraminifera assemblage, which indicate glacial conditions and a shallow marine depositional environment, respectively (Courtillat *et al.*, 2020). An assignment of MIS6 age for the interval conflicts with the interpretation of Courtillat *et al.* (2020), who report a hiatus just below the *E. huxleyi* datum from 330 to 120 ka (MIS5d to MIS10) based, *inter alia*, on the absence of *Globigerinoides ruber* pink at Site U1461. However, considering the near absence of planktonic foraminifera in the ooid-rich sections (Courtillat *et al.*, 2020), the absence of *G. ruber* pink might be a facies effect rather than representing a real gap in sedimentation. The resulting age model presented here implies that one hiatus at *ca* 15 m is separating MIS2 from MIS6 while another hiatus just below the *E. huxleyi* datum at *ca* 18.65 m is separating MIS6 from MIS10 sediments (Fig. 2).

A more extensive age model, including the upper 1000 m (*ca* 6 Ma), was recently published for Site U1461 (He *et al.*, 2021). Below the radiocarbon age limit, extending down to 100 m depth, the presented age–depth relationship is based on lithological properties. It is proposed that light-coloured aragonitic sections correlate to arid glacial conditions, whereas relatively dark-coloured calcitic sediments form during humid interglacial periods. Following this assumption, glacial and interglacial periods are assigned consecutively based on the repeated occurrence of colour changes observed in core (He *et al.*, 2021). The age model of He *et al.* (2021) thereby ignores the existence of biostratigraphic datums (Gallagher *et al.*, 2017b; Courtillat *et al.*, 2020) and the occurrence of extended periods of non-deposition at Site U1461 (Courtillat *et al.*, 2020). In effect, resulting ages of He *et al.* (2021) contradict those presented here and by Courtillat *et al.* (2020).

Depositional environment

At Site U1461, XRF-based climate proxies indicate a depositional environment characterized by alternating arid glacial and humid interglacial conditions during the last *ca* 500 kyr (Fig. 2). Sedimentological data show that arid intervals are dominated by aragonite-needle mud and non-skeletal grains, while humid periods are characterized by bioclastic calcite dominated sediments with a higher siliciclastic fraction (Fig. 2). This confirms observations of Hallenberger *et al.* (2019) who showed that a rapid increase in fluvial runoff at 10 ka led to a shelf-wide cessation of the precipitation and deposition of inorganic aragonite. Before 10 ka, during the Last Glacial Maximum (LGM) and post-LGM sea-level rise, the formation of inorganic aragonite was facilitated by an arid climate, a lack of fluvial influx and an associated elevated aragonite saturation state (Hallenberger *et al.*, 2019). After 10 ka, shelf sedimentation was instead of predominantly calcitic mineralogy and of biogenic origin (James *et al.*, 2004;

Hallenberger *et al.*, 2019). Data presented here implies a strong association between regional climate and the general mode of production of shelf carbonates, extending back to at least 500 ka.

Additional evidence for the existence of these two opposing carbonate factories can be found in isotope data. Aragonite-rich sediments are much heavier in oxygen and carbon isotopes as compared with bioclastic calcitic carbonates (Fig. 6). This trend is in part the result of differences in carbonate mineralogy. Aragonite produced by precipitation from seawater is enriched in $\delta^{13}C$ (+1.6‰) as compared to calcite (Weber & Woodhead, 1969; Swart *et al.*, 2009). A similar, albeit smaller, fractionation has been reported for oxygen isotopes of laboratory-grown aragonite and calcite (+0.6‰) (Tarutani *et al.*, 1969).

However, differences in isotope values exceed simple trends in mineralogy, indicating that additional factors influenced fractionation between the different facies (Fig. 6). Further control is enacted by the primary isotopic composition of the seawater from which the carbonates precipitate. On a global scale, the oxygen isotopic composition of seawater varies based on the polar ice volume. Ice preferentially incorporates the light oxygen isotope (^{16}O) resulting in an enrichment in ^{18}O within the remaining water. This implies higher expected oxygen isotope ratios of carbonates formed during glacials as compared to interglacials (Adkins *et al.*, 2002). Thus, if data is to be compared to present-day conditions, a shift of approximately −0.1‰ for 10 m of glacioeustatic sea-level fall needs to be applied to account for the differences in ice-volume (Fig. 6) (Swart, 2015). This shift is most significant for shallow marine ooids, which are thought to have formed at Site U1461 during high amplitude sea-level lowstands (−120 m).

Water temperature and variations thereof are a well-known and important influence on the oxygen isotopic composition of carbonates (Swart, 2015). At the NWS, sea surface temperatures are reduced by up to 3°C during glacial periods in comparison to warmer interglacials (Barrows & Juggins, 2005). However, water depths are considerably lower at the studied site during glacial lowstands (<10 m). The overall reduction in glacial temperatures at Site U1461 is therefore potentially compensated by the coeval decrease in water depth.

Locally, the balance of evaporation and precipitation further controls the isotopic composition. During evaporation, ^{16}O is preferentially removed from the seawater, resulting in a heavier $\delta^{18}O$ signature. This response is also known as 'salinity effect' due to the covariant increase in seawater salinity (Swart *et al.*, 2009). Similarly, the carbon isotope ratio of seawater likely increased during glacials due to the shallow and restricted nature of the depositional environment. Fractionation occurs by photosynthesis, which preferably incorporates light carbon (^{12}C) in organic matter (Lazar & Erez, 1992). The remaining bicarbonate pool becomes enriched in ^{13}C resulting in a heavier carbon isotope composition (Swart *et al.*, 2009).

All of the above summarized trends are in accordance with the proposed differences in palaeoenvironment and climate between carbonates which formed during humid interglacials and arid glacials. Elevated salinity and a more restricted seawater exchange during the formation of aragonite-rich sediments led to an enrichment of heavy oxygen and carbon isotopes as opposed to the interglacial hemipelagic and calcite-rich sediments. This is in line with the low sea-level and elevated alkalinity indicated by the occurrence of superficial ooids. Similar effects have been observed in coastal waters of Qatar and the sedimentary record of the Great Australian Bight, where measured $\delta^{18}O$ and $\delta^{13}C$ become heavier with increasing restriction and evaporation (Rivers *et al.*, 2009, 2019).

In comparison to other contemporary shallow marine tropical carbonates, ooids/peloids described here display similar values to those deposited across the present-day Great Bahama Bank or the Kuwait Ramp (Fig. 6). This reinforces the assumption that a more restricted environment characterized shallow marine conditions at the NWS during glacials. Isotope data of ooids and aragonite-needle mud further compares well with similar sediments presently found at the ocean floor across large parts of the NWS (Fig. 6). This implies that the prevailing palaeoenvironmental conditions between stranded sediments of late Pleistocene to Holocene age and older strata studied here are comparable.

Arid glacials – shallow marine platforms

The exact depth range and conditions within which tropical ooids form are an ongoing topic of debate (Harris *et al.*, 2019). However, most literature agrees on the necessity of very shallow marine conditions (<5 mwd) and elevated alkalinities to promote the growth of ooids (Simone, 1980; Harris *et al.*, 2019). During high amplitude lowstands, including MIS12, MIS6 and MIS2, Site U1461 (presently 127 mwd) was situated in very shallow water depths (<10 mwd) and characterized by an arid climate (Fig. 2). This created suitable conditions for the lithification of peloids and the development of ooids (Hallenberger *et al.*, 2019). These conditions were shortlived, which is expressed by the superficial nature of ooids and the limited extent of shallow water deposits in seismic data (Platforms 1 and 2; Fig. 8). The close spatial association with unconformities (U1 to U3; Fig. 8) further indicates a low relative sea-level during the three major episodes of ooid formation. In each case, the seismic-reflection data reveals the existence of an erosional surface landward of the ooid-rich sections. Considering the present-day water depth over the mid-ramp to outer ramp section (Fig. 8), these parts of the shelf were only exposed briefly during high amplitude lowstands, such as MIS12, MIS6 and MIS2 (Miller *et al.*, 2005). The unconformities U3, U2 and U1 are therefore interpreted to represent exposure during the MIS12-lowstand, MIS6-lowstand and MIS2-lowstand, respectively.

Benthic foraminifera, including *A. gaimardii*, *P. verriculata* and *E. craticulatum,* are typically present wherever ooids occur at Site U1461 (Courtillat *et al.*, 2020). This fossil assemblage is interpreted to represent shallow marine inner ramp conditions, thereby supporting the proposed origin of ooids (Courtillat *et al.*, 2020). The pervasive co-occurrence of these benthic foraminifera further indicates that ooids formed *in situ*, rather than being transported to Site U1461.

The oldest ooids recorded in this study formed on a small-scale progradational platform (Platform 1). The age of this platform is interpreted to be equivalent to MIS12, which represents a prolonged period of low sea-level (−120 mwd; Miller *et al.*, 2005) and mostly arid climate (Stuut *et al.*, 2014). The end of the platform development is marked by the deposition of a thin layer of grainstone (Facies 4). The origin of these sediments is somewhat ambiguous, because it represents a singularity within the studied core (Fig. 3). Climate records indicate that humid conditions already prevailed near the end of the MIS12 lowstand (Fig. 2) (Stuut *et al.*, 2014). The resulting palaeoenvironment might have been analogous to the present-day inner ramp, where sedimentation is characterized by a similar assemblage of coarse skeletal sands (Dix, 1989; James *et al.*, 2004). Thus, if glacioeustatic sea-level rise lags changes in climate, parts of the mid-ramp to outer ramp might be briefly transformed into depositional environments, which resemble present-day inner ramp conditions at the NWS.

Following MIS12, ooids only reoccur at Site U1461 within much younger sediments deposited during the MIS6 glacial (Fig. 2). This lack of active ooid production at the studied site is attributed to the sea-level evolution, which results in water depths persistently above 10 m during MIS11 to MIS7 (Fig. 2) (Miller *et al.*, 2005). During the MIS6 lowstand, shallow marine ooids developed again at Site U1461. These deposits formed on top of a small-scale platform (Platform 2), which displays a strong resemblance in position and size to the older MIS12 platform (Fig. 8). This appears reasonable, considering the similar palaeoenvironmental conditions present, including a low water depth (<10 m) and arid climate (Fig. 2). An important difference between the two platforms is represented by their respective age of formation. The MIS12 platform (Platform 1) exhibits shallow marine carbonate production during a single glacial lowstand. In contrast, Platform 3 exhibits an amalgamation of sediments formed and deposited during the MIS6 and MIS2 lowstand, with an extended period of non-deposition in between (Figs 2 and 9). The interpretation of this hiatus is mainly based on published age data for Site U1461. Additionally, low sedimentation rates are indicated by the local occurrence of intraclasts and stained non-skeletal grains containing authigenic minerals such as pyrite (Fig. S1). Similar stained deposits have been described for the Central Southern Australian Margin (James *et al.*, 1997; Rivers *et al.*, 2007). There, they represent Pleistocene relict grains currently stranded at the seafloor due to low Holocene sedimentation rates (Rivers *et al.*, 2007). Landward of Site U1461, parts of Platform 2 display signs of subaerial erosion and/or karstification associated with the MIS2 lowstand (U3; Fig. 8). Based on the development of the relative sea-level, exposure was likely limited to a short period during the Last Glacial Maximum (LGM), when sea-level was at its lowest point of −125 m (Yokoyama *et al.*, 2001; Ishiwa *et al.*, 2019a).

In contrast to Site U1461, well-developed ooids are reported from core data of industry well BHC4 and at IODP Site U1462 (Gallagher *et al.*, 2014, 2018). These locations are situated 100 km north-east of Site U1461, in shallower present-day water depths of about 80 m (Fig. 1). During prolonged periods of intermediate lowstand conditions, flat-topped aggradational to progradational platforms developed across extended parts of the contemporary mid-ramp (Goktas *et al.*, 2016; Gallagher *et al.*, 2018). Landward of Site U1461, the mid-ramp section is comparatively narrow and characterized by serrated and discontinuous reflectors (Fig 8). These features, which are interpreted as karstification, prevent a concise interpretation. However, the presence of structures including internal downlap and progradation of single sigmoidal reflectors can be observed (Platform 3; Fig. 8). These structures might indicate the development of a small-scale carbonate platform, which lies between two unconformities (U2 and U3). Both unconformities become conformable and merge towards the distal part of the seismic section (CC2 and CC3). At Site U1461, they are associated with the lowstand deposits formed during MIS2 and MIS6 (Fig. 8). Considering the palaeoenvironmental conditions necessary for ooid formation on the NWS (Gallagher *et al.*, 2018; Hallenberger *et al.*, 2019), the platform likely developed during MIS3 to MIS4. This period was characterized by prolonged intermediate relative sea-level, shifting large parts of the present-day mid-ramp section into shallower water depths (Fig. 9). In addition, the climate was arid during this period (Stuut *et al.*, 2014), favouring the formation of inorganic precipitated platform carbonates such as ooids (Fig. 2). During consecutive lowstands, parts of the shelf were exposed and subject to karstification. This causes the high amplitude contrasts of reflectors observed landward of Site U1461 as well as on older platforms across the NWS (Fig. 9) (Gallagher *et al.*, 2014, 2018).

Arid glacials – hemipelagic sedimentation

The origin of aragonite-needle mud formed at the NWS was linked to the occurrence of ‘whiting’ events, comparable to those presently taking place at the Bahamas or the Persian Gulf (Dix *et al.*, 2005; Hallenberger *et al.*, 2019). This interpretation agrees with the observed size and shape of aragonite-needles (Fig. 4E), which indicate formation by precipitation from seawater rather than being derived from the breakdown of calcareous algae (Macintyre & Reid, 1992). The term ‘whiting’ is commonly applied to describe metre-scale to kilometre-scale patches of milky-white suspended material occurring predominantly in shallow marine tropical to subtropical environments (Broecker & Takahashi, 1966; Shinn *et al.*, 1989). Their exact origin is an ongoing topic of debate, with most models favouring either bio-induced or entirely inorganic precipitation of aragonitic fine-material close to the sea surface (Robbins & Blackwelder, 1992; Purkis *et al.*, 2017). Suggested environmental conditions include an elevated aragonite saturation state, which is commonly the result of shallow marine conditions and an arid climate (Shinn *et al.*, 1989; Robbins & Blackwelder, 1992; Purkis *et al.*, 2017). These conditions fit the proposed palaeoenvironment of the NWS during dry glacials (Fig. 2). Following modern and past analogues (Shinn *et al.*, 1989; Purkis *et al.*, 2017), the formation of aragonite-needle mud at the NWS is proposed to have occurred in very shallow marine conditions. However, the NWS represents a truly open marine environment with strong tidal currents and unimpeded wave energy (Dix, 1989; James *et al.*, 2004). Therefore, much of the fine material was likely transported off-shelf and settled in deeper water. This is corroborated by the presence of pelagic skeletal grains including coccolithophorids and planktonic foraminifera (Fig. 4F). The depositional history of aragonite-needle mud, including a shallow marine formation and subsequent export, is further reflected in its benthic foraminiferal assemblage. The dominant species, including *C. lobatulus*, *G. prageri* and *R. spinulos*, are typical for mid-ramp to outer ramp conditions (Courtillat *et al.*, 2020). In addition, *P. pertusus* and *P. exigue* occur exclusively within the aragonite-needle mud facies (Courtillat, 2019). *Peneroplis pertusus* typically occurs on the innermost carbonate ramp and is often most abundant in hypersaline environments (Parker & Gischler, 2015). In the Exmouth Gulf, on the inner ramp of the NWS, *P. pertusus* and *P. exigue* are common and show an increased abundance towards shallower water (Orpin *et al.*, 1999). This supports the idea that aragonite needles precipitated in hypersaline shallow-water environments but were later exported to deeper water where they mixed with pelagic carbonates.

The oldest sequence of aragonitic micrite deposited at Site U1461 is represented by a 20 m thick interval, which is matched to MIS10, an extended period of intermediate to low sea-level and arid conditions (Fig. 2) (Stuut *et al.*, 2014; Courtillat *et al.*, 2020). Seismic-reflection data reveals equivalent thicknesses achieved over large parts of the studied outer ramp to

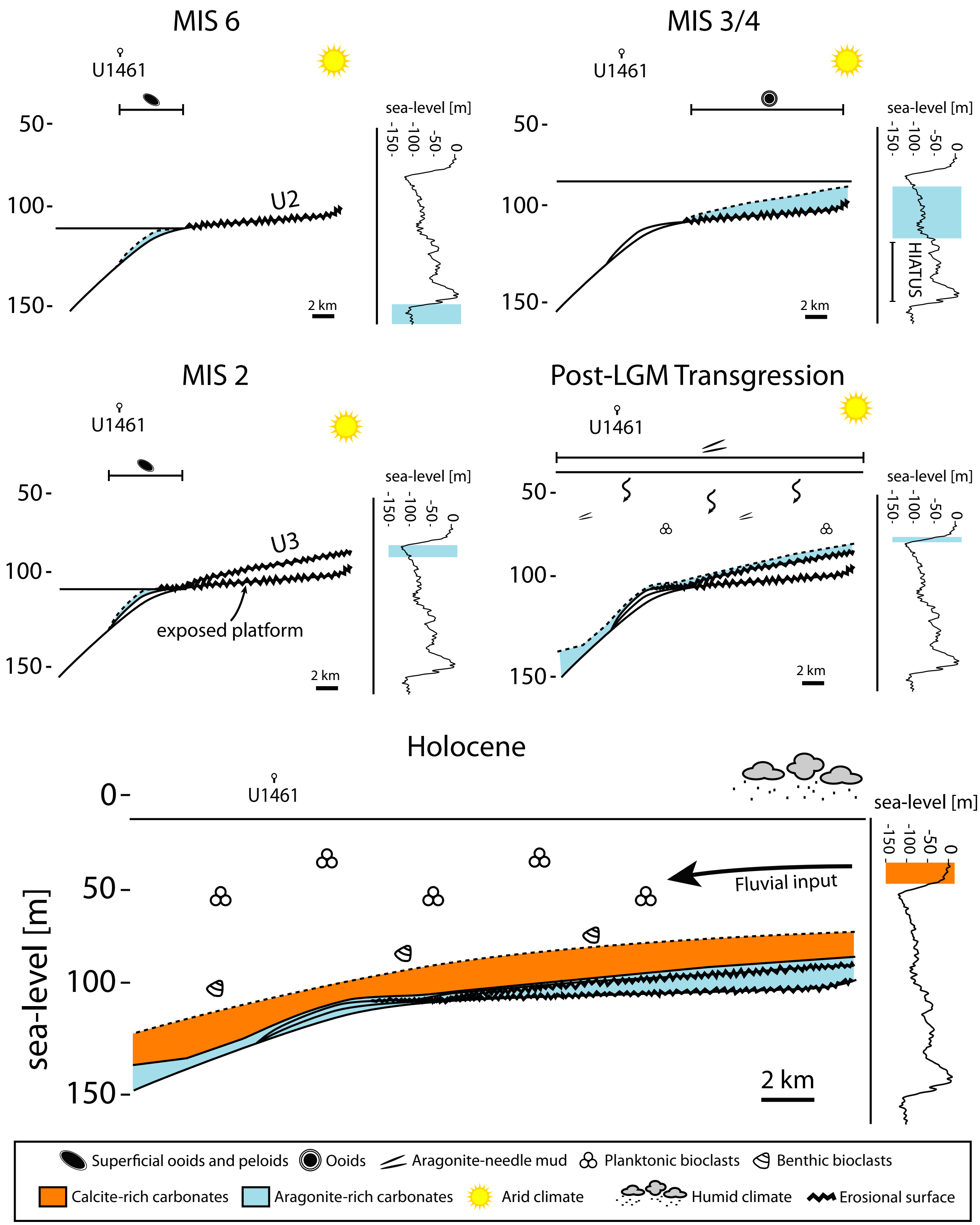
MIS 6
U1461
U2
50-
100-
150-
sea-level [m]
0-
-50-
-100-
-150-
2 km
MIS 3/4
U1461
HIATUS
MIS 2
U1461
U3
exposed platform
Post-LGM Transgression
U1461
Holocene
U1461
0-
Fluvial input
sea-level [m]
Superficial ooids and peloids
Ooids
Aragonite-needle mud
Planktonic bioclasts
Benthic bioclasts
Calcite-rich carbonates
Aragonite-rich carbonates
Arid climate
Humid climate
Erosional surface

Fig. 9. The evolution of the present-day mid-ramp to outer ramp at Site U1461 over the last 200 kyr in response to climate and glacioeustatic sea-level changes (Miller *et al.*, 2005). (Marine Isotope Stage – MIS – 6) Large parts of the shelf were exposed during lowstand conditions resulting in karstification and subaerial erosion (U2). During the later stages of MIS6, an arid climate and shallow marine conditions led to superficial ooid and peloid formation at Site U1461. (MIS5). The MIS5 interglacial is missing in core and seismic, suggesting a prolonged hiatus. (MIS3/4) This extended period was characterized by an arid climate and intermediate sea-levels, when a shallow-marine flat-topped platform developed landward of Site U1461. (MIS2) The lowstand conditions present during the Last Glacial Maximum (LGM) led to a second pulse of superficial ooid formation at Site U1461. The platform that developed during MIS3/4 was exposed and subject to karstification (U3). (Post-LGM Transgression) Aragonitic mud composed of fine needles formed and deposited over large parts of the shelf during the post-LGM transgression. Deposition post-dates sea-level rise, which progressively flooded larger areas of the Northwest Shelf (NWS). (Holocene) After 10 ka, sedimentation switched rapidly into a mixture of pelagic and benthic skeletal fragments with a calcitic mineralogy. This change was associated with increased humidity and terrigenous material influx (Hallenberger *et al.*, 2019). In contrast, large parts of the present-day mid-ramp preserve minor or no active sedimentation during this period (James *et al.*, 2004).

mid-ramp section, indicating a potentially large accumulation of hemipelagic sediments during glacial periods (Fig. 8). However, the exact conditions of deposition, especially in relation to the sea-level evolution, remain ambiguous due to a lack of age constraint (Fig. 2). The timing of hemipelagic glacial carbonate deposition is better constrained for the well-dated late Pleistocene to Holocene aragonite-needle mud deposited at Site U1461. This 1 m thick interval formed during the last post-glacial transgression when the shelf became increasingly submerged (Fig. 9). The resulting transgressive deposits cover large areas of the mid to outer ramp, as shown by the present-day distribution of stranded aragonite mud (Dix *et al.*, 2005).

Considering the palaeoenvironment, 'whiting' related aragonite-needle mud likely formed during all arid lowstands and transgressions. Yet, several glacial stages are missing at Site U1461, including MIS3 and MIS4 (Fig. 2). During glacial lowstands, limited amounts of the shelf were covered by water (Ward *et al.*, 2013). Given that present-day 'whitings'; largely occur over shallow parts of the platform (Shinn *et al.*, 1989; Purkis *et al.*, 2017), the production of aragonite mud might have been limited. The lower relative sea-level also meant that large parts of the submerged shelf were affected by unimpeded wave energy and strong tidal currents. It is therefore feasible that newly formed aragonite mud was exported into deeper water, potentially bypassing the shelf entirely. Similar processes have been described for the Middle Miocene carbonate ramp of the Great Bahama Bank. There, shallow-water aragonite needles are interpreted to have been actively exported into deeper water by hydrodynamic processes (Turpin *et al.*, 2011). In addition, fine material that formed and deposited during periods of intermediate sea-level was potentially remobilized during consecutive lowstands. For example, whiting-related aragonite mud that was deposited on the present-day outer ramp during MIS3 and MIS4 would have been transported offshore after the following glacioeustatic sea-level fall during MIS2. Evidence of this process is shown by prominent onlap structures seaward of Site U1461 that might indicate the presence of material that was deposited during the LGM (Fig. 8). In addition to winnowing, aragonite-needle mud might have been reworked by bioturbation due to bottom grazing organisms. This is suggested by the composition of faecal pellets, which are almost entirely composed of small needles identical to those in the aragonitic mudstones (Fig. 4D and F).

Humid interglacials

Today, sedimentation across the NWS is mostly limited to an outer ramp pelagic ridge and the inner ramp. The absence of Holocene sedimentation is thought to be caused by a combination of low primary productivity and a constant reworking of sediment by unimpeded currents, storm waves and a strong seaward flow of saline bottom waters (James *et al.*, 2004; Dix *et al.*, 2005).

At Site U1461, a relatively thick succession of Holocene strata is present (Figs 3 and 9). Based on their composition, these sediments are comparable to the pelagic sands, which are presently accumulating along the outer ramp of the NWS where they form a linear sediment ridge following the continental margin (Jones, 1973; James *et al.*, 2004). However, the lateral extent of this 20 km wide ridge is not matched in the seismic line (Fig. 8). Instead, Holocene sediments blanket large areas of the mid-ramp to outer ramp (Fig. 8). The presence of this thick sequence of Holocene strata may be due to the proximity of Barrow Island and adjacent elevated areas (Fig. 1). Modelling results suggest that these seabed features strongly modify current energy, resulting in a highly heterogeneous distribution of bottom stress across the surrounding shelf (Condie *et al.*, 2006; Condie & Andrewartha, 2008). At Site U1461, seabed geometry acts as a local baffle, greatly reducing bottom stress across the mid-ramp to outer ramp (Condie *et al.*, 2006; Condie & Andrewartha, 2008). Simultaneously, current energy is enhanced across other parts of the shelf. This is exemplified by the presence of a contemporaneous subaquatic sediment-wave field located 8 km north-east of Site U1461 (Belde *et al.*, 2017). These bedforms are composed of coarse material and occur in areas where the current energy is comparatively high (Belde *et al.*, 2017). The dominant orientation of dune crests (north-west/south-east) further implies that sediment is actively transported into the direction of the studied site (Belde *et al.*, 2017), where it then settles due to the strong decrease in current energy (Condie & Andrewartha, 2008). Therefore, significant sediment accumulation occurred in parts of the mid-ramp to outer ramp during interglacials whenever sufficient shelter was present.

However, these conditions are not likely to have existed during every interglacial in the last 500 kyr, because sediments formed during interglacial highstands are relatively uncommon. At Site U1461, MIS11 is the only other interglacial stage with a thickness of bioclastic-rich sediments comparable to Holocene deposits. During the Holocene and MIS11, upwelling periods connected to productivity maxima have been reported offshore Cape Range, Northwest Australia (Spooner *et al.*, 2011). These maxima are related to a reduction in mixed layer thickness due to an enhanced Australian Summer Monsoon (Spooner *et al.*, 2011). Nevertheless, elevated primary productivity is not likely to be the main factor determining enhanced sedimentation during interglacials on the mid-ramp to outer ramp. If this were the case, 'low-productivity' interglacials would be characterized by fluvial derived terrigenous material accumulation. Yet, such condensed sections are not present at Site U1461 (Fig. 3). The presence of interglacial sedimentation is instead proposed to be dominantly controlled by local changes in current strength. Under present-day conditions, seabed stress in the Dampier Island area may vary by an order of magnitude on a kilometre-scale (Condie & Andrewartha, 2008). This heterogeneity is likely to adjust as a response to past variations in the underlying seafloor morphology. During interglacials where strata are missing (MIS5, MIS7 and MIS9), the mid-ramp to outer ramp section was likely subjected to strong currents which led to off-shelf or along-shelf transportation of sediment. In this regard, the NWS may be compared to the 'shaved shelf' of the Great Australian Bight, where Holocene skeletal carbonates are transported off-shelf during the Holocene (James *et al.*, 1994; Rivers *et al.*, 2007). Additionally, past interglacial sediments are potentially remobilized or eroded after their initial deposition during consecutive lowstands. Evidence for this process can be found in the more proximal parts of MIS11 deposits, where seismic data indicates the existence of karstification and erosion of time equivalent sediments (Fig. 8).

Implications

Facies belts on shallow marine tropical ramps often display a typical transition from oolitic grainstone into skeletal packstone followed by outer ramp mudstone, representing an increasing distance from the shore and a progressive decrease in energy (e.g. Tucker & Wright, 1990). At a cursory glance, the presented successions observed in core could therefore be interpreted as simple transgressive or regressive trends, expressing the vertical stacking of laterally adjacent facies ("Walther's Law"). Instead, this study reveals the existence of two mutually exclusive carbonate factories, which switch cyclically in accord with orbital controlled changes in regional climate. During arid glacials, abiotic processes result in the formation of aragonite-needle mud and non-skeletal grains. By contrast, humid interglacials are characterized by condensed accumulation of biotic calcite.

In addition, glacioeustatic changes in sea-level modify depositional patterns. Fluctuations in relative sea-level may result in the exposure or drowning of previously active small-scale platforms, the remobilization of fine-grained carbonates during regressions, or the deposition of large amounts of transgressive sediments blanketing previous lowstand deposits. Thus, a strong allogenic control is present at the NWS. Autogenic factors are further known to influence sedimentary systems and may result in the creation of complex and repetitive stratigraphy (Burgess & Wright, 2003; Burgess, 2006). At the studied parts of the mid-ramp to outer ramp, observed autogenic control is largely limited to local differences in the bottom stress resulting in sediment trapping downcurrent of bathymetric highs.

In summary, the presented research on the NWS indicates a predictable cyclicity in carbonate sedimentation as a response to (mostly) climate forcing, a connection which may be present in ancient carbonate ramps developed during icehouse climates. These observations have implications for the creation and evaluation of reservoir models concerning similar systems. During glacial lowstands, shallow marine platforms developed repeatedly on the present-day outer and mid-ramp (Fig. 8). Depending on their diagenetic pathway, these deposits may yield considerable porosities and therefore represent potential exploration targets. Especially early meteoric overprint has been shown to be highly effective in creating high porosities, a process which was observed in comparable platforms studied at the NWS (Gallagher *et al.*, 2018). During transgression, these platforms readily drown and are blanketed by hemipelagic sediments, including aragonite-needle mud and calcitic bioclastic carbonates. Throughout early diagenesis, these fine-grained sediments will lose considerable amounts of porosity due to compaction and/or aragonite-to-calcite transformation (Melim *et al.*, 2002). Beginning trends of the preferential removal of (micro)porosity can already be observed in the upper 70 m of Site U1461 (Fig. 7). Thus, a trap may form over large parts of the observed ramp system, including the glacial-lowstand platforms.

Changes in the carbon isotopic composition of carbonates are often interpreted to reflect perturbations in the global carbon cycle (Shackleton & Pisias, 1985; Hayes *et al.*, 1999). Data presented here displays elevated δ^{13}C values in glacials as compared to interglacial deposits, for example, a marked increase in δ^{13}C is observed at the transition from the LGM to the Holocene (Fig. 3). In contrast, open ocean records from tropical latitudes do not show the same signal, but rather indicate little change in δ^{13}C of surface-marine carbonates during this time (Peterson *et al.*, 2014). Discrepancies between the open ocean carbon isotope record and periplatform sites have been documented previously for several carbonate platform and ramp systems across the world (Swart, 2008). These patterns are linked to the variable mixing of neritic, relatively ^{13}C-rich and aragonite-rich sediments with calcite-rich, pelagic sediments representing a lighter δ^{13}C signature (Swart & Eberli, 2005; Swart, 2008). Generally, this is in accordance with the observations at Site U1461, showing elevated δ^{13}C values in the neritic, aragonite-dominated intervals (Fig. 3). However, Swart (2008) linked the heavier carbon isotope values to periods of relative sea-level highstands, arguing that aragonite export to deeper waters is increased when the shelf is flooded ('highstand shedding'). In contrast, ^{13}C-rich, aragonitic sediments on the NWS are produced and exported during arid glacials and therefore out of phase with the carbonate platforms described by Swart (2008). The NWS record demonstrates that changes in aridity can be as effective as sea-level in controlling carbon isotope variability in carbonate platform settings. Thus, δ^{13}C records in platform margin carbonates should only be interpreted in combination with all available sedimentological data to understand the underlying factors controlling the observed carbonate system and its relationship to the observed isotope signal.

CONCLUSIONS

The integration of core and seismic analysis shows that non-skeletal aragonite-rich sediments alternate with hemipelagic, calcite-rich sediments over the last 500 kyr at Site U1461. Regional climate is interpreted as the main control for these two contrasting carbonate factories. During periods of extended aridity (glacial stages) shelf sedimentation was dominated by inorganic precipitated aragonite-needle mud and non-skeletal grains.

At the studied site, most humid interglacials during the last 500 kyr are characterized by reduced sedimentation. However, the mid-shelf to outer shelf section surrounding the area north-west of Dampier Island preserves evidence of sedimentation occurring during the Holocene and Marine Isotope Stage 11 interglacial. At Site U1461, these interglacials are represented by biogenic-derived calcite with an elevated fluvial influx from terrigenous sources. This presence of thick interglacial units is related to adjacent offshore barriers, which modified the otherwise strong energy flux of tidal currents. As a result, considerable amounts of sediment are trapped downcurrent of bathymetric highs.

Large parts of the Northwest Shelf are at present sediment-starved, indicating that shelf growth largely took place during arid glacials. Considering the extensive size of the 600 km wide shelf, aragonitic lowstand deposits potentially constitute volumes that rival classic highstand-systems such as the Bahamas. These stacks of aragonitic sediment, either localized as flat-topped platforms or widespread in the form of aragonite-needle mud, have a large diagenetic potential. The distribution and timing of sediments formed during arid glacials therefore has important implications for the creation of carbonate ramp and carbonate reservoir models.

ACKNOWLEDGEMENTS

This study was performed on samples collected during IODP Expedition 356 (Indonesian Throughflow) and was supported by a grant of the German Science foundation (DFG, RE 2697/4-1). We thank the JRSO (JOIDES Resolution Science Operator) staff and the Siem Offshore crew for their invaluable assistance and skill during Expedition 356. The Australian IODP office and the ARC Basin Genesis Hub (IH130200012) provided funding to Stephen Gallagher. The German Federal Ministry of Education and Research (BMBF grant 03G0257A) provided funding for the *R/V Sonne* expedition SO257-WACHEIO. We thank one anonymous reviewer and Julie Kupecz for their constructive reviews. We would further like to thank *Sedimentology* editor Eric Hiatt for summarizing and commenting on the reviews. Uwe Wollenberg and Philipp Binger (RWTH Aachen University) are thanked for their support in creating XRD and thin-section data. EasyCompany is gratefully acknowledged for providing the EasyCore software under an Academic User License Agreement. We also like to thank IHS Markit for providing Kingdom Suite as part of an Academic User License Agreement. Open Access funding enabled and organized by Projekt DEAL.

DATA AVAILABILITY STATEMENT

The data that support the findings of this study are openly available in a 'Pangea' repository at https://doi.org/10.1594/PANGAEA.927008, https://doi.org/10.1594/PANGAEA.927012, https://doi.org/10.1594/PANGAEA.927013, https://doi.org/10.1594/PANGAEA.927014, https://doi.org/10.1594/PANGAEA.927015, https://doi.org/10.1594/PANGAEA.927017, and https://doi.org/10.1594/PANGAEA.927018.

REFERENCES

Adkins, J.F., **McIntyre, K.** and **Schrag, D.P.** (2002) The salinity, temperature, and δ18O of the glacial deep ocean. *Science*, **298**, 1769–1773.

Australian Bureau of Metereology (2000) *Climate Statistics of the Barrow Island Metereological Station*. Australian Bureau of Metereology, Melbourne.

Barrows, T.T. and **Juggins, S.** (2005) Sea-surface temperatures around the Australian margin and Indian Ocean during the Last Glacial Maximum. *Quatern. Sci. Rev.*, **24**, 1017–1047.

Belde, J., **Reuning, L.** and **Back, S.** (2017) Bottom currents and sediment waves on a shallow carbonate shelf, Northern Carnarvon Basin, Australia. *Cont. Shelf Res.*, **138**, 142–153.

Broecker, W.S. and **Takahashi, T.** (1966) Calcium carbonate precipitation on the Bahama Banks. *J. Geophys. Res.*, **71**, 1575–1602.

Burchette, T.P. and **Wright, V.P.** (1992) Carbonate ramp depositional systems. *Sediment. Geol.*, **79**, 3–57.

Burgess, P.M. (2006) The signal and the noise: forward modeling of allocyclic and autocyclic processes influencing peritidal carbonate stacking patterns. *J. Sediment. Res.*, **76**, 962–977.

Burgess, P.M. and **Wright, V.P.** (2003) Numerical forward modeling of carbonate platform dynamics: An evaluation of complexity and completeness in carbonate strata. *J. Sediment. Res.*, **73**, 637–652.

Condie, S., **Andrewartha, J.**, **Mansbridge, J.** & **Waring, J.** (2006) *Modelling circulation and connectivity to Australia's North West Shelf. Hobart, Tas.* CSIRO Marine and Atmospheric Research; Government of Western Australia, Perth, W.A.

Condie, S. and **Andrewartha, J.** (2008) Circulation and connectivity on the Australian North West shelf. *Cont. Shelf Res.*, **28**, 1724–1739.

Cook, H.E. and **Taylor, M.E.** (1991) Carbonate-slope failures as indicators of sea-level lowerings. *AAPG Bulletin*, **75**, 556.

Courtillat, M. (2019) *Reconstruction des changements océanographiques et atmosphériques dans l'Océan Indien Oriental (NO-Australie, IODP Exp 356) pendant le quaternaire*. Université de Pepignan, Francais.

Courtillat, M., **Hallenberger, M.**, **Bassetti, M.-A.**, **Aubert, D.**, **Jeandel, C.**, **Reuning, L.**, **Korpanty, C.**, **Moissette, P.**, **Mounic, S.** and **Saavedra-Pellitero, M.** (2020) New Record of Dust Input and Provenance During Glacial Periods in Western Australia Shelf (IODP Expedition 356, Site U1461) from the Middle to Late Pleistocene. *Atmosphere*, **11**, 1251.

Deik, H., **Reuning, L.**, **Petrick, B.** and **Takayanagi, H.** (2019) Hardened feacal pellets as a significant component in deep water, subtropical marine environments. *Depositional Rec*, **5**, 348–361.

Dix, G.R. (1989) High-energy, inner shelf carbonate facies along a tide-dominated non-rimmed margin, northwestern Australia. *Mar. Geol.*, **89**, 347–362.

Dix, G.R., **James, N.P.**, **Kyser, T.K.**, **Bone, Y.** and **Collins, L.B.** (2005) Genesis and dispersal of carbonate mud relative to late quaternary sea-level change alogn a distally-steepened carbonate ramp (Northwester Shelf, Western Australia). *J. Sediment. Res.*, **75**, 665–678.

Eberli, G.P. and **Ginsburg, R.N.** (1987) Segmentation and coalescence of Cenozoic carbonate platforms, northwestern Great Bahama Bank. *Geology*, **15**, 75–79.

Flügel, E. (2013) *Microfacies of Carbonate Rocks: Analysis, Interpretation and Application*. Springer Science & Business Media, Berlin.

Gallagher, S.J., **Fullthorpe, C.S.**, **Bogus, H.** and **Scientists, T.E.** (2017a) Expedition 356 methods. In: *Proceedings of the International Ocean Discovery Program* (Eds Gallagher, S.J., Fulthorpe, C.S. and Bogus, K.), International Ocean Discovery Program, College Station, TX.

Gallagher, S.J., **Fullthorpe, C.S.**, **Bogus, H.** and **Scientists, T.E.** (2017b) Site U1461. In: *Proceedings of the International Ocean Discovery Program* (Eds Gallagher, S.J., Fulthorpe, C.S. and Bogus, K.), International Ocean Discovery Program, College Station, TX.

Gallagher, S.J., **Reuning, L.**, **Himmler, T.**, **Henderiks, J.**, **De Vleeschouwer, D.**, **Groeneveld, J.**, **Rastegar Lari, A.**, **Fulthorpe, C.S.**, **Bogus, K.**, **Renema, W.**, **McGregor, H.V.**, **Kominz, M.A.**, **Auer, G.**, **Baranwal, S.**, **Castañeda, S.**, **Christensen, B.A.**, **Franco, D.R.**, **Gurnis, M.**, **Haller, C.**, **He, Y.**, **Ishiwa, T.**, **Iwatani, H.**, **Jatiningrum, R.S.**, **Korpanty, C.A.**, **Lee, E.Y.**, **Levin, E.**, **Mamo, B.L.**, **McHugh, C.M.**, **Petrick, B.F.**, **Potts, D.C.**, **Takayanagi, H.** and **Zhang, W.** (2018) The enigma of rare Quaternary oolites in the Indian and Pacific Oceans: A result of global oceanographic physicochemical conditions or a sampling bias? *Quatern. Sci. Rev.*, **200**, 114–122.

Gallagher, S.J., **Wallace, M.W.**, **Hoiles, P.W.** and **Southwood, J.M.** (2014) Seismic and stratigraphic evidence for reef expansion and onset of aridity on the Northwest Shelf of Australia during the Pleistocene. *Mar. Pet. Geol.*, **57**, 470–481.

Gischler, E. (1994) Sedimentation on three Caribbean atolls: glovers reef, Lighthouse reef and Turneffe islands, Belize. *Facies*, **31**, 243.

Gischler, E. (2003) Holocene lagoonal development in the isolated carbonate platforms off Belize. *Sed. Geol.*, **159**, 113–132.

Gischler, E. and **Lomando, A.J.** (2005) Offshore sedimentary facies of a modern carbonate ramp, Kuwait, northwestern Arabian-Persian Gulf. *Facies*, **50**, 443–462.

Goktas, P., **Austin Jr, J.A.**, **Fulthorpe, C.S.** and **Gallagher, S.J.** (2016) Morphologies and depositional/erosional controls on evolution of Pliocene-Pleistocene carbonate platforms: Northern Carnarvon Basin, Northwest Shelf of Australia. *Cont. Shelf Res.*, **124**, 63–82.

Haak, A.B. and **Schlager, W.** (1989) Compositional variations in calciturbidites due to sea-level fluctuations, late Quaternary, Bahamas. *Geol. Rundsch.*, **78**, 477–486.

Hallenberger, M., **Reuning, L.**, **Gallagher, S.J.**, **Back, S.**, **Ishiwa, T.**, **Christensen, B.A.** and **Bogus, K.** (2019) Increased fluvial runoff terminated inorganic aragonite precipitation on the Northwest Shelf of Australia during the early Holocene. *Sci. Rep.*, **9**, 1–9.

Harris, P., **Diaz, M.R.** and **Eberli, G.P.** (2019) The formation and distribution of modern ooids on Great Bahama Bank. *Ann. Rev. Marin Sci.*, **11**, 491–516.

Hayes, J.M., **Strauss, H.** and **Kaufman, A.J.** (1999) The abundance of 13C in marine organic matter and isotopic fractionation in the global biogeochemical cycle of carbon during the past 800 Ma. *Chem. Geol.*, **161**, 103–125.

He, Y., **Wang, H.** and **Liu, Z.** (2021) Development of the Leeuwin Current on the northwest shelf of Australia through the Pliocene-Pleistocene period. *Earth Planet. Sci. Lett.*, **559**, 116767.

Hengesh, J., **Dirstein, J.** and **Stanley, A.** (2013) Landslide geomorphology along the Exmouth plateau continental margin, North West Shelf, Australia. *Aust. Geomech.*, **48**, 71–92.

Hesse, P.P., **Magee, J.W.** and **van der Kaars, S.** (2004) Late Quaternary climates of the Australian arid zone: a review. *Quatern. Int.*, **118**, 87–102.

IODP-MI (2011) *IODP Depth Scale Terminology version 2.0*. IODP-MI, College Station, TX.

Ishiwa, T., **Yokoyama, Y.**, **Okuno, J.**, **Obrochta, S.**, **Uehara, K.**, **Ikehara, M.** and **Miyairi, Y.** (2019a) A sea-level plateau preceding the Marine Isotope Stage 2 minima revealed by Australian sediments. *Sci. Rep.*, **9**, 1–8.

Ishiwa, T., **Yokoyama, Y.**, **Reuning, L.**, **McHugh, C.M.**, **De Vleeschouwer, D.** and **Gallagher, S.J.** (2019b) Australian Summer Monsoon variability in the past 14,000 years revealed by IODP Expedition 356 sediments. *Prog. Earth Planet. Sci.*, **6**, 17.

James, N.P., **Bone, Y.**, **Hageman, S.J.**, **Feary, D.** and **Gostin, V.A.** (1997) *Cool-Water Carbonate Sedimentation During the Terminal Quaternary Sea-Level Cycle*. Lincoln Shelf, Adelaide, SA.

James, N.P., **Bone, Y.**, **Kyser, T.K.**, **Dix, G.R.** and **Collins, L.B.** (2004) The importance of changing oceanography in controlling late Quaternary carbonate sedimentation on a high-energy, tropical, oceanic ramp: north-western Australia. *Sedimentology*, **51**, 1179–1205.

James, N.P., **Boreen, T.D.**, **Bone, Y.** and **Feary, D.A.** (1994) Holocene carbonate sedimentation on the west Eucla Shelf, Great Australian Bight: a shaved shelf. *Sed. Geol.*, **90**, 161–177.

Jones, H.A. (1973) *Marine Geology of the Northwest Australian Continental Shelf*. Bureau of Mineral Resources, Geology and Geophysics, Canberra, ACT.

Lazar, B. and **Erez, J.** (1992) Carbon geochemistry of marine-derived brines: I. 13C depletions due to intense photosynthesis. *Geochim. Cosmochim. Acta*, **56**, 335–345.

Logan, B.W., **Read, J.F.** and **Davies, G.R.** (1970) *History of Carbonate Sedimentation, Quaternary Epoch, Shark Bay, Western Australia*. Department of Geology (University of Western Australia), Perth.

Macintyre, I.G. and **Reid, R.P.** (1992) Comment on the origin of aragonite needle mud: a picture is worth a thousand words. *J. Sediment. Res.*, **62**, 1095–1097.

Melim, L.A., **Westphal, H.**, **Swart, P.K.**, **Eberli, G.P.** and **Munnecke, A.** (2002) Questioning carbonate diagenetic paradigms: evidence from the Neogene of the Bahamas. *Mar. Geol.*, **185**, 27–53.

Miller, K.G., **Kominz, M.A.**, **Browning, J.V.**, **Wright, J.D.**, **Mountain, G.S.**, **Katz, M.E.**, **Sugarman, P.J.**, **Cramer, B.S.**, **Christie-Blick, N.** and **Pekar, S.F.** (2005) The Phanerozoic record of global sea-level change. *Science*, **310**, 1293–1298.

Orpin, A., **Haig, D.** and **Woolfe, K.** (1999) Sedimentary and foraminiferal facies in Exmouth Gulf, in arid tropical northwestern Australia. *Aust. J. Earth Sci.*, **46**, 607–621.

Parker, J.H. and **Gischler, E.** (2015) Modern and relict foraminiferal biofacies from a carbonate ramp, offshore Kuwait, northwest Persian Gulf. *Facies*, **61**, 10.

Peterson, C.D., **Lisiecki, L.E.** and **Stern, J.V.** (2014) Deglacial whole-ocean δ13C change estimated from 480 benthic foraminiferal records. *Paleoceanography*, **29**, 549–563.

Purdy, E.G. (1963) Recent calcium carbonate facies of the Great Bahama Bank. 2. Sedimentary Facies. *J. Geol.*, **71**, 472–497.

Purkis, S., **Cavalcante, G.**, **Rohtla, L.**, **Oehlert, A.M.**, **Harris, P.M.** and **Swart, P.K.** (2017) Hydrodynamic control of whitings on Great Bahama Bank. *Geology*, **45**, 939–942.

Purser, B. and **Evans, G.** (1973) Regional sedimentation along the Trucial coast, SE Persian Gulf. In: *The Persian Gulf* (Ed. Purser, B.), pp. 211–231. Springer, Berlin.

Raffi, I., **Wade, B.**, **Pälike, H.**, **Beu, A.**, **Cooper, R.**, **Crundwell, M.**, **Krijgsman, W.**, **Moore, T.**, **Raine, I.** and **Sardella, R.** (2020) The Neogene Period. In: *Geologic Time Scale 2020* (Eds Gradstein, F.M., Ogg, J.G., Schmitz, M.D. and Ogg, G.M.), pp. 1141–1215. Elsevier, Amsterdam.

Rankey, E.C., **Garza-Perez, R.** and **Eltom, H.A.** (2021) Chemical oceanographic influences on sediment accumulations of a carbonate ramp: Holocene Yucatan Shelf, Mexico. *Sedimentology*, **68**, 324–351.

Read, J.F. (1985) Carbonate platform facies models. *AAPG Bulletin*, **69**, 1–21.

Rivers, J.M., **James, N.P.**, **Kyser, T.K.** and **Bone, Y.** (2007) Genesis of palimpsest cool-water carbonate sediment on the continental margin of southern Australia. *J. Sediment. Res.*, **77**, 480–494.

Rivers, J.M., **Kyser, T.K.** and **James, N.P.** (2009) Isotopic composition of a large photosymbiotic foraminifer: Evidence for hypersaline environments across the Great Australian Bight during the late Pleistocene. *Sed. Geol.*, **213**, 113–120.

Rivers, J.M., **Varghese, L.**, **Yousif, R.**, **Whitaker, F.F.**, **Skeat, S.L.** and **Al-Shaikh, I.** (2019) The geochemistry of Qatar coastal waters and its impact on carbonate sediment chemistry and early marine diagenesis. *J. Sediment. Res.*, **89**, 293–309.

Robbins, L. and **Blackwelder, P.** (1992) Biochemical and ultrastructural evidence for the origin of whitings: a biologically induced calcium carbonate precipitation mechanism. *Geology*, **20**, 464–468.

Schlager, W. (1991) Depositional bias and environmental change—important factors in sequence stratigraphy. *Sed. Geol.*, **70**, 109–130.

Schlager, W. (2003) Benthic carbonate factories of the Phanerozoic. *Int. J. Earth Sci.*, **92**, 445–464.

Schlager, W., **Reijmer, J.J.** and **Droxler, A.** (1994) Highstand shedding of carbonate platforms. *J. Sediment. Res.*, **64**, 270–281.

Shackleton, N.J. and **Pisias, N.** (1985) Atmospheric carbon dioxide, orbital forcing, and climate. In: *The Carbon Cycle and Atmospheric CO2: Natural Variations Archean to Present* (Eds Sundquist, E.T. and Broecker, W.S.), Volume. **32**, pp. 303–317. American Geophysical Union, Washington, DC.

Shinn, E.A., **Steinen, R.P.**, **Lidz, B.H.** and **Swart, P.K.** (1989) Whitings, a sedimentologic dilemma. *J. Sediment. Res.*, **59**, 147–161.

Simone, L. (1980) Ooids: a review. *Earth Sci. Rev.*, **16**, 319–355.

Smodej, J., **Reuning, L.**, **Wollenberg, U.**, **Zinke, J.**, **Pfeiffer, M.** and **Kukla, P.A.** (2015) Two-dimensional X-ray diffraction as a tool for the rapid, nondestructive detection of low calcite quantities in aragonitic corals. *Geochem. Geophys. Geosyst.*, **16**, 3778–3788.

Spooner, M.I., **De Deckker, P.**, **Barrows, T.T.** and **Fifield, L.K.** (2011) The behaviour of the Leeuwin Current offshore NW Australia during the last five glacial–interglacial cycles. *Global Planet. Change*, **75**, 119–132.

Stuut, J.W., **Temmesfeld, F.** and **De Deckker, P.** (2014) A 550 ka record of aeolian activity near North West Cape, Australia: inferences from grain-size distributions and bulk chemistry of SE Indian Ocean deep-sea sediments. *Quatern. Sci. Rev.*, **83**, 83–94.

Swart, P.K. (2008) Global synchronous changes in the carbon isotopic composition of carbonate sediments unrelated to changes in the global carbon cycle. *Proc. Natl Acad. Sci.*, **105**, 13741–13745.

Swart, P.K. (2015) The geochemistry of carbonate diagenesis: The past, present and future. *Sedimentology*, **62**, 1233–1304.

Swart, P.K. and **Eberli, G.** (2005) The nature of the δ13C of periplatform sediments: Implications for stratigraphy and the global carbon cycle. *Sed. Geol.*, **175**, 115–129.

Swart, P.K., **Reijmer, J.J.** and **Otto, R.** (2009) A reevaluation of facies on great Bahama Bank II: Variations in the Δ13 C, Δ18 O and mineralogy of surface sediments. In: *Perspectives in Carbonate Geology: A Tribute to the Career of Robert Nathan Ginsburg* (Eds Swart, P.K., Eberli, G.P. and McKenzie, J.A.), pp. 47–59. International Association of Sedimentologists, Ghent

Tarutani, T., **Clayton, R.N.** and **Mayeda, T.K.** (1969) The effect of polymorphism and magnesium substitution on oxygen isotope fractionation between calcium carbonate and water. *Geochim. Cosmochim. Acta*, **33**, 987–996.

Thomson, J., **Croudace, I.** and **Rothwell, R.** (2006) A geochemical application of the ITRAX scanner to a sediment core containing eastern Mediterranean sapropel units. *Geol. Soc., London, Spec. Public.*, **267**, 65–77.

Tucker, M.E. and **Wright, V.P.** (1990) *Carbonate Sedimentology*. John Wiley & Sons, Hoboken, NJ.

Turpin, M., **Emmanuel, L.**, **Reijmer, J.J.** and **Renard, M.** (2011) Whiting-related sediment export along the Middle Miocene carbonate ramp of Great Bahama Bank. *Int. J. Earth Sci.*, **100**, 1875–1893.

Ward, I., **Larcombe, P.**, **Mulvaney, K.** and **Fandry, C.** (2013) The potential for discovery of new submerged archaeological sites near the Dampier Archipelago, Western Australia. *Quatern. Int.*, **308**, 216–229.

Ward, W.C. and **Brady, M.J.** (1973) *High-energy Carbonates on the Inner Shelf, Northeastern Yucatan Peninsula, Mexico*. Gulf Coast Association of Geological Societies, Austin, TX.

Weber, J.N. and **Woodhead, P.M.** (1969) Factors affecting the carbon and oxygen isotopic composition of marine carbonate sediments—II. Heron Island, Great Barrier Reef, Australia. *Geochim. Cosmochim. Acta*, **33**, 19–38.

Yokoyama, Y., **De Deckker, P.**, **Lambeck, K.**, **Johnston, P.** and **Fifield, L.K.** (2001) Sea-level at the Last Glacial Maximum: evidence from northwestern Australia to constrain ice volumes for oxygen isotope stage 2. *Palaeogeogr. Palaeoclimatol. Palaeoecol.*, **165**, 281–297.

Manuscript received 12 October 2020; revision accepted 15 September 2021

Supporting Information

Additional information may be found in the online version of this article:

Fig. S1. (A) Backscattered scanning electron microscopy (BSE) imaging of a single non-skeletal grain reveals the existence of a dense serrated cortex surrounding the ooid. In plain sight, these ooids are characterized by dark discoloration, U1461C-2H-5W-44 cm, 15.84 m. (B) and (C) Based on energy dispersive X-ray spectroscope (EDX) elemental mapping, it can be determined that the dense areas of (A) predominantly consist of iron (Fe) and sulphur (S), likely representing the presence of pyrite.

Fig. S2. (A) The linear regression between porosity and acoustic impedance displays a strong negative relationship ($r = -0.9$, $P = 6.033 \times 10^{-16}$). (B) By comparison, there is no significant relationship between grain density and acoustic impedance ($r = -0.17$, $P > 0.05$).

Table S1. Oxygen and carbon isotope record measured on bulk sediment and non-skeletal grains. All values are reported in per mil (‰) relative to the Vienna Pee Dee Belemnite (VPDB) according to the delta notation. Depth is expressed as common metres composition (CCSF-A).